ABSTRACT

BIOMECHANICAL STUDY OF PERFORMANCE OF A PLUGGED FEMORAL IMPLANT COUPLED WITH A TROCHANTER CABLE SYSTEM USING FINITE ELEMENT ANALYSIS

by
Deanna Yvonne Carstarphen

A Finite Element Analysis was conducted to determine the effect of a plug on the performance of the critical section of a femoral implant coupled with a trochanter cable grip system. The critical section was defined near the proximal end of the stem where a hole was designed for the purpose of attaching the cable grip system. Two models were generated for the analysis. One consisted of the critical section with the grip cables and a plug filled in the hole and the other was without the plug. The models were based on design specifications provided by Howmedica Incorporated. Two types of simulations were performed on each model. The static simulation represented the instant the hip is subjected to full "heel strike" loading conditions during a normal walking cycle. The quasi-dynamic simulations represented two critical sub-phases of stance ("heel strike" and "foot flat") where the maximum loads were exerted on the implant. A normal walking speed of 4 km/h was used in the analysis. The cables around the hole were pre-tensioned.

Both static and quasi-dynamic results showed that the von Mises stress concentrations in the plugged model were lower than those in the non-plugged model. That is, a plug added to the hole of a femoral implant adjoined with a cable grip system reduced the critical stress around the hole. In addition, stress distributions within the implant were also altered due to the plug: it shifted the stress concentration away from the hole. Thus, these led to an enhancement in the performance of the implant.

BIOMECHANICAL STUDY OF PERFORMANCE OF A PLUGGED FEMORAL IMPLANT COUPLED WITH A TROCHANTER CABLE SYSTEM USING FINITE ELEMENT ANALYSIS

by
Deanna Yvonne Carstarphen

A Thesis
Submitted to the Faculty of
New Jersey Institute of Technology
in Partial Fulfillment of the Requirements for the Degree of
Master of Science in Mechanical Engineering

Department of Mechanical Engineering

August 1999

APPROVAL PAGE

BIOMECHANICAL STUDY OF PERFORMANCE OF A PLUGGED FEMORAL IMPLANT WITH A TROCHANTER CABLE GRIP SYSTEM USING FINITE ELEMENT ANALYSIS

Deanna Yvonne Carstarphen

Dr. Taiming (Tina) Chu, Thesis Advisor — Date
Assistant Professor of Mechanical Engineering, NJIT

Mr. Michael W. Dudasik, Committee Member — Date
Product Development Engineer, Howmedica Incorporated, Rutherford, NJ

Dr. J. Russell Parsons, Committee Member — Date
Associate Professor, UMDNJ-NJMS

BIOGRAPHICAL SKETCH

Author: Deanna Yvonne Carstarphen

Degree: Master of Science in Mechanical Engineering

Date: August 1999

Undergraduate and Graduate Education:

- Master of Science in Mechanical Engineering
  New Jersey Institute of Technology, Newark, NJ 1999

- Bachelor of Science in Mechanical Engineering,
  Rutgers, The State University, College of Engineering, Piscataway, NJ, 1997

Major: Mechanical Engineering

This thesis is dedicated to the Almighty Yahweh
and my family: Marguerite, Yvonne, Lafica and Mark.
Thank you for your love and support.

ACKNOWLEDGEMENT

I would like to express my sincere appreciation to my thesis advisor, Dr. Taiming (Tina) Chu, for her support throughout this research. Special thanks are given to Mr. Michael Dudasik and Dr. J. Russell Parsons for serving as members of the committee. An additional thank you is given to Mr. Michael Dudasik of Howmedica Incorporated for providing information and assistance throughout the research.

Finally, I would like to thank Dr. Ronald Kane, Dean of Graduate Studies of NJIT and the National Consortium for Minorities in Engineering and Science (GEM) for providing funding to participate in this research.

TABLE OF CONTENTS

TABLE OF CONTENTS
(Continued)

Chapter **Page**

TABLE OF CONTENTS
(Continued)

Chapter **Page**

LIST OF TABLES

LIST OF TABLES
(Continued)

LIST OF FIGURES

LIST OF FIGURES
(Continued)

Figure **Page**

CHAPTER 1

INTRODUCTION

1.1 Background

Total hip arthroplasty is considered to be one of the successful procedures for alleviating pain and restoring function in the arthritic hip (Tarr 1982; Cheal et al. 1992). In this procedure, a metal implant is inserted into the proximal end of the femur and fixed (Fig. 1.1). The choice of the implant is based on patient selection, surgical technique, material properties and basic biomechanical principles.

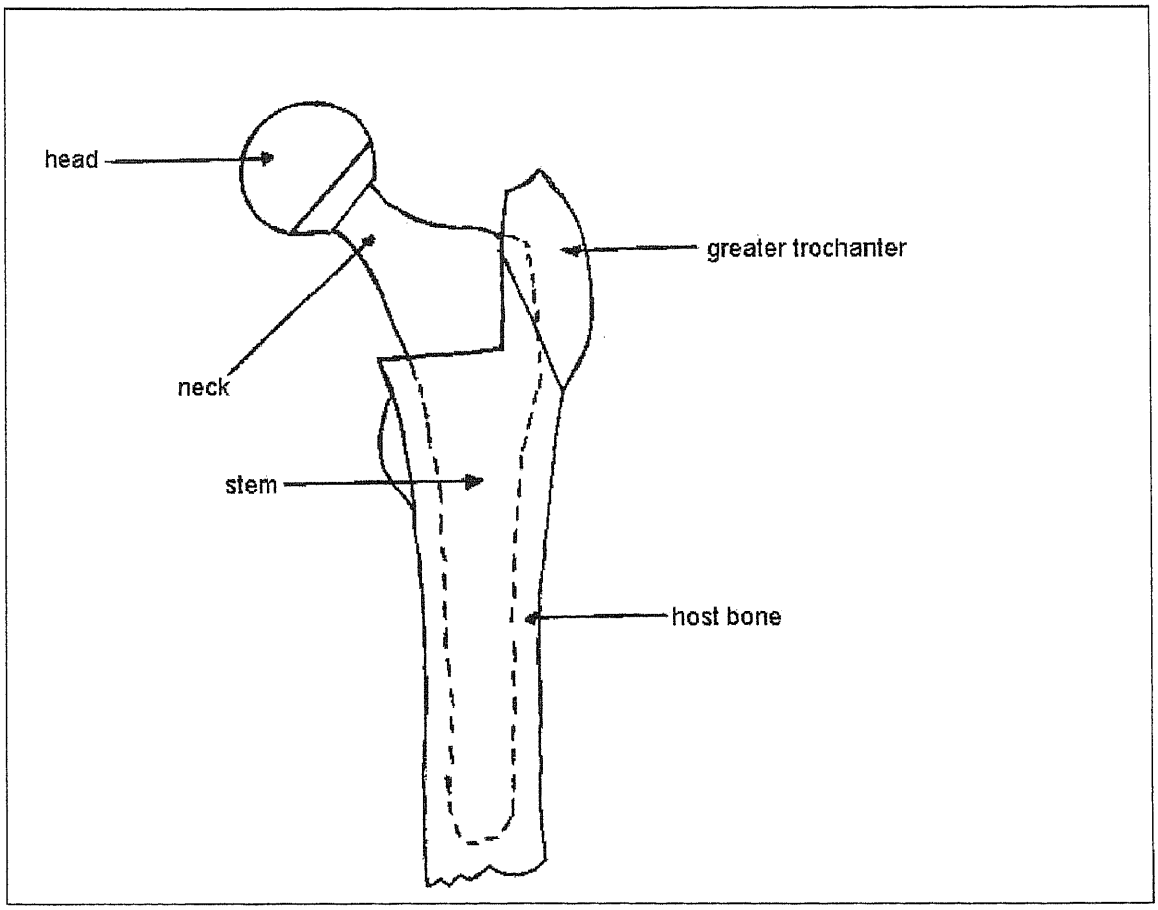

Figure 1.1 Femoral implant attached to the femur.

In a scenario where the host bone of the patient is weak, surgeons must ensure that the bone does not entirely support the loading environment of the implant. This is achieved by augmenting the implant with a cable grip system. This system is commonly known as the Dall-Miles Cable Grip System (DMCGS). Howmedica Incorporated currently manufactures this device. In this procedure (Fig. 1.2), two cobalt-chromium cables are: (1) threaded through a pre-drilled hole in a titanium alloy implant (called the "Head-Neck Replacement"), (2) wrapped around the greater trochanter of the femur, (3) threaded through a mounted cable grip, (4) secured through pre-tensioning and (5) crimped at the ends with cable sleeves. As a result, the loading environment of the implant is shifted from the weak host bone to the cables.

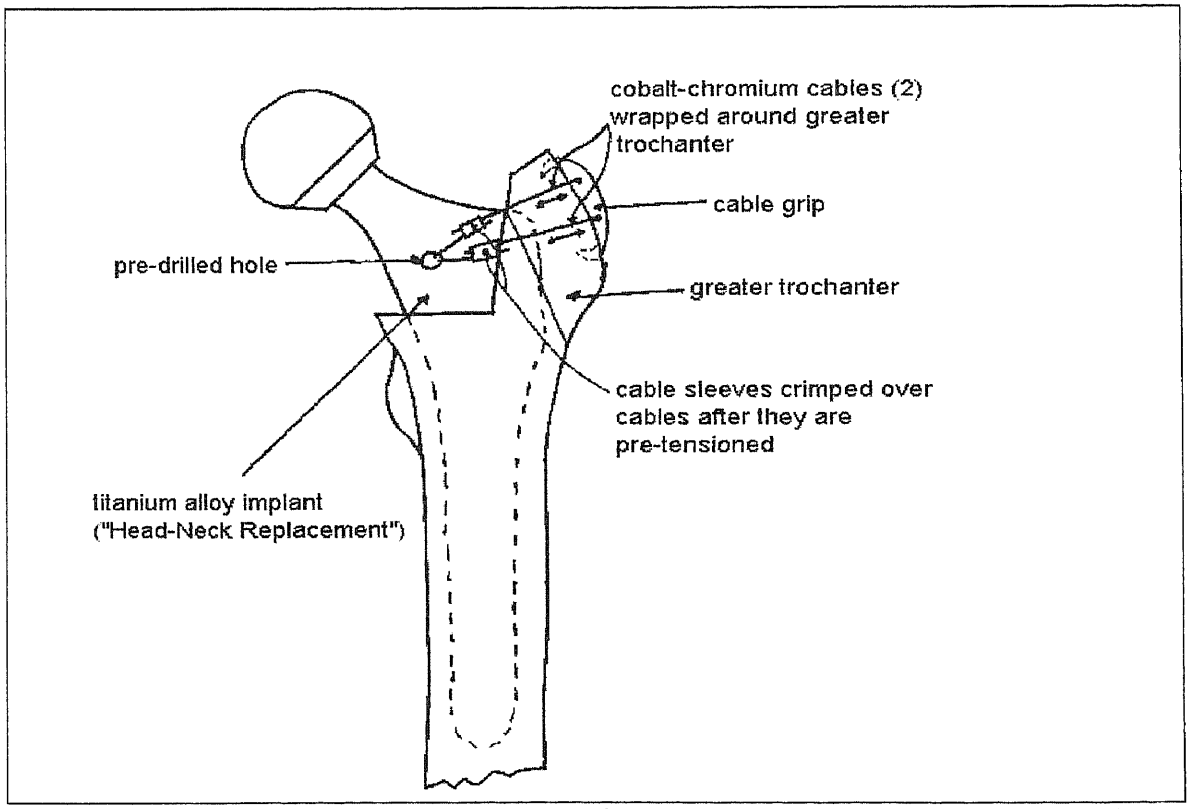

Figure 1.2 Femoral implant attached to the femur adjoined with the Dall-Miles Cable Grip System. *Courtesy of Howmedica Incorporated.*

1.2 Problem Statement

The issue of concern with the application of the Dall-Miles Cable Grip System (DMCGS) to the Head-Neck Replacement (HNR) is the stress concentrations in the implant at the hole where the cables are threaded (Fig. 1.2). These stress concentrations are the result of geometric stress factors such as notches, holes, and grooves that cause an increase in stress at the surface of the geometry (Juvinall and Marshek 1991). Moreover, contact stresses exist due to the application of a large load over a small surface area. Situations of this nature are found whenever a force is transmitted through bodies in contact (Ugural and Fenster 1995c). In the current study, the geometric stress factor is due to the presence of the hole. Contact stresses are generated between the cables and the implant at those areas where the tensile force is applied parallel to the surface of the implant (along the direction of the cables) inside of the hole.

1.3 Need

A graduate project at the New Jersey Institute of Technology in Newark, NJ involved a Finite Element Analysis (FEA) of performance of a femoral implant, coupled with the Dall-Miles Cable Grip System, with a cobalt-chromium plug filled in at the hole (Jung et al. 1997). The plug represented a design modification concept, developed by Howmedica Inc., in an effort to reduce the stress concentrations in the implant around the hole. Two simple models of the implant stem were created and analyzed. One represented the stem with the plug in the hole and the other without the plug. A preliminary static simulation was performed on each model. The simulation represented a normal standing condition of the hip. The preliminary results of the project showed that the geometric stress

concentration in the model with the plug was lower than that in the model without the plug.

Since the models created in the previous project did not include the cables from the Dall-Miles Cable Grip System, the preliminary results only showed the effect of the plug on the *geometric stress concentrations* in the implant due to the presence of the hole. They did not show the plug's effect on the *contact stress* between the cables and the implant on the inside of the hole. Moreover, the preliminary results only illustrated the effect of the plug on the *static* performance of the implant. No dynamic simulations were used to determine the effect of the plug on implant performance as the hip undergoes motion.

The project of Jung et al. (1997) provided a step towards solving the stress concentration problem in femoral implants coupled with grip cables. The current investigation is an in depth study of the previous project, which seeks to obtain detailed and additional information about the effect of the plug on modified femoral implant performance that was not evident in the previous project. The current study includes static and quasi-dynamic simulations of the stance phase of a normal walking cycle.

1.4 Objective

The purpose of this investigation is to determine, in detail, the effect of a cobalt-chromium plug on the performance of a titanium alloy femoral implant adjoined with cobalt-chromium cables from an attached Dall-Miles Cable Grip System (DMCGS). The purpose of using the plug is to reduce the stress concentrations in the implant around the hole where the cables are threaded.

1.5 Specific Aims

The specific aims of this investigation are as follows:

- to develop a three-dimensional solid model of the critical section of two titanium alloy femoral implants each coupled with two cobalt-chromium grip cables; one model consists of the critical section with the plug in the hole and the other is without the plug,
- to develop an optimal finite element mesh for each model using appropriate boundary conditions and convergence,
- to determine the effect of the plug on the performance of the implant (due to the effect of the cables) under both static and quasi-dynamic conditions and
- to compare the results (both static and quasi-dynamic) between the plugged and non-plug models.

1.6 Significance

The information obtained from the current investigation provides Howmedica Incorporated with detailed insight into the effect of their new design modification concept (the plug) on their current femoral implant design (the Head-Neck Replacement adjoined with the Dall-Miles Cable Grip System). Such insight also better aids in the development of an optimal femoral implant design that can restore hip function in arthritic patients.

CHAPTER 2

LITERATURE SURVEY

In the literature to date, there is an absence of studies on performance of modified femoral implants adjoined with cable grip systems for correction of the arthritic hip. Based on conversations with Michael Dudasik (a Product Development Engineer at Howmedica Incorporated), the current study represents the first investigation on this subject.

The following sections provide a literature review of relevant topics for the current study, which include femoral implant stem and cable geometry, the Finite Element method, joint and muscle loading of the femur during walking and properties of common materials used in femoral implants and cables. The purpose of reviewing these topics is to gain insight into the development of a suitable model for the Finite Element Analysis (FEA) of the current investigation.

2.1 Geometry

2.1.1 Femoral Implant Stems

The basic geometry of femoral implant stems includes length, contours of corners and edges and cross-section, which is critical from a surgical and mechanical point of view. The surgical factor affected by stem geometry is the ease of insertion and removal. The mechanical factors affected include the allowance for proper fixation, stress concentrations and general stress transfer as determined by axial, shear, flexural and torsional loading.

The choice of appropriate length of the stem is based primarily on surgical indications. The surgeon weighs factors such as ease of insertion versus ease of removal. If the stem is too short, loosening of the implant may occur. On the other hand, long stems are difficult to insert or remove during surgery. Stem lengths ranging between 100 mm and 300 mm (4 in. and 12 in.) are considered acceptable lengths for femoral implant stems (Tarr 1982).

The contour of the stem determines its orientation within the bone canal. According to Tarr (1982), straight stem implants are becoming more common because such implants are neutrally oriented and easily inserted or removed during surgery. Moreover, for cement applications, such contours reduce the possibility of air pocket development at the implant-cement interface by allowing a complete covering of cement around the stem.

The choice of implant designs intended to reduce critical stress development within the cement can contribute to a prolonged implant service life. Several investigations of cemented implant stems have been performed to determine optimal cross-sectional geometry for the stem. Figure 2.1 illustrates the effect of stem cross-section geometry on cement stresses as determined by Crowninsheild et al. (1980) in their study of stem cross-section design. As Fig. 2.1 shows, the cross-section represented by geometry D produces the lowest amount of cement stresses.

Femoral implant designs intended to reduce critical stress development at the bone-implant interface of cementless implants have also been investigated. According to Walker and Robertson (1988), cementless implants offer several potential advantages over cemented ones, including reduced operating time, long-term interface stability and ease of revision. There are two common types of cementless fixation of implants, which

facing page 7

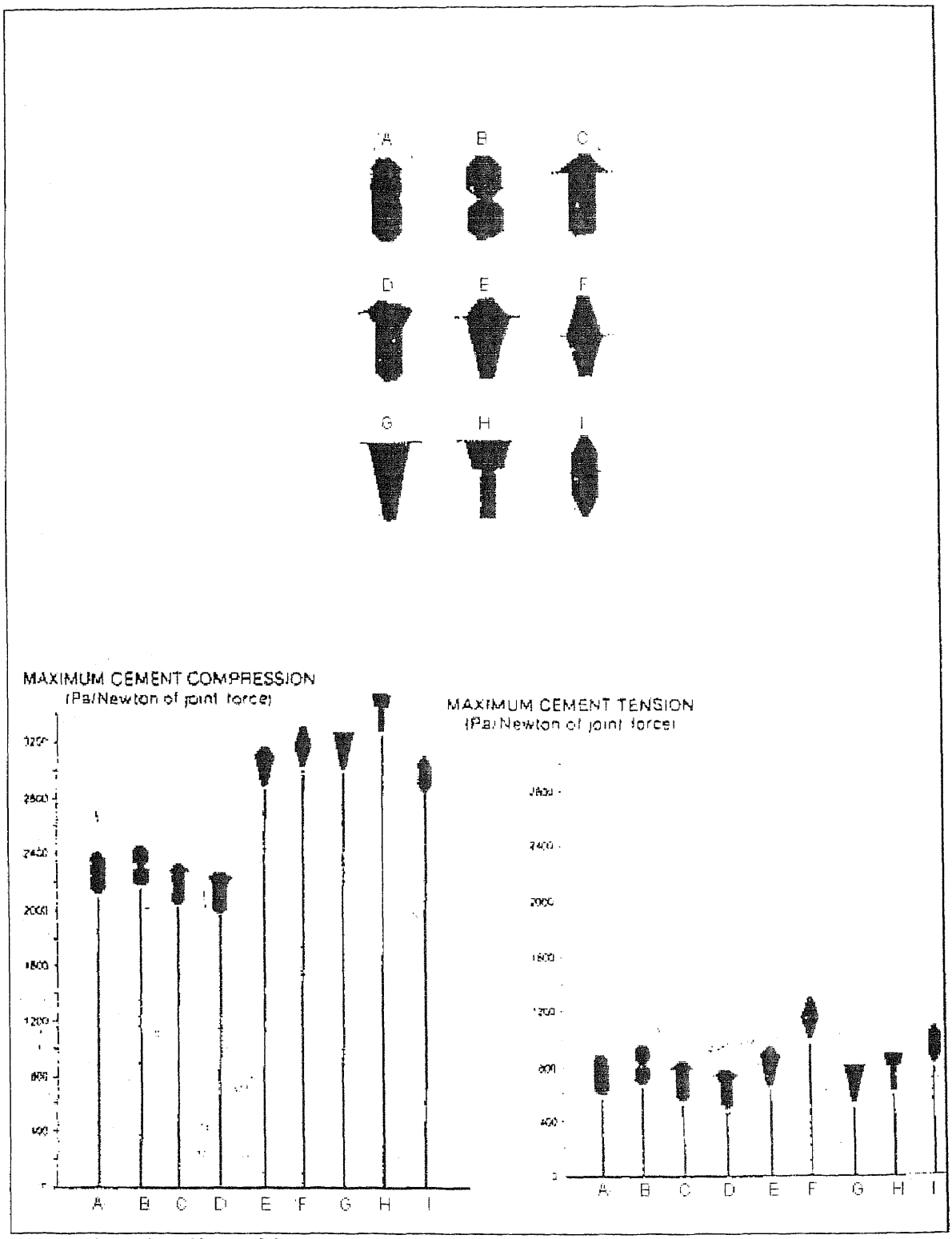

Figure 2.1 The effect of femoral implant stem cross-section geometry on cement stresses. Source: R. D. Crowninsheild, R. A. Brand, R. C. Johnson, and J. C. Milroy. 1980. "The Effect of Femoral Stem Cross-Sectional Geometry on Cement Stresses in Total Hip Reconstruction." *Clin. Orthop. Rel. Res.* 146: 71-77.

include the "press-fit" stem and the "coated" stem (Walker and Robinson 1988). A "press fit" stem is one where the implant is made slightly larger than the femur's canal. The interference between the stem and the bone provides the stability. In a "coated" stem, a three-dimensional coating is applied to the implant. The bone in contact with the coating grows into it and anchors the implant.

2.1.2 Cables

Cables are commonly used in orthopaedic surgery to reattach bone fragments for the fixation of various types of internal fractures (Park 1979). Due to the need of a solution to the weak host bone problem in arthritic hip patients, Howmedica Inc. developed a technique such that cables could also be used in hip femoral replacement surgery to aid in the correction of arthritis. The basic geometry of cables is diameter size and physical configuration. The surgical and mechanical factors affected by cable geometry are ease of cable passage, stress concentrations and tensile strength.

The choice of an appropriate cable size is based on several factors. Cables designed for ease of passage require small diameters (Winter et al. 1980b). On the other hand, small cable diameters contribute to small surface areas, which produce contact stresses in systems where cables are in contact with other materials (Ugural and Fenster 1995c).

The physical configuration of cables is classified in terms of monofilament and twisted or braided multifilament (Winter et al. 1980b). Physical configuration affects the tensile strength of cables along the filament. Multifilament cables generally exhibit higher tensile strengths than monofilament cables (Ratner et al. 1996c). However, a disadvantage to using the multifilament configuration in cable design is the tendency of

crevice (interface formed between two or more components) corrosion to occur between the filaments (Winter et al. 1980b). This can cause decreases in filament diameter over time creating undesired stress concentrations along the cable.

2.2 The Finite Element Method

In a numerical simulation of a physical process, one employs a numerical method and a computer to evaluate a mathematical model of the process. The Finite Element (FE) method is considered to be a successful numerical technique for evaluating complex physical processes in various types of orthopaedic systems (Huiskes and Hollister 1993). The FE method has been used extensively (Rohlmann et al. 1983; Cheal et al. 1992; Rotem 1994) to model hip replacements due to the ease with which parameters such as material properties, loads and constraints can be varied. However, this method has not been used to model hip replacements coupled with cable grip systems.

2.2.1 Features

Three features (Reddy 1993a) characterize the FE method:

1. The domain of the model is represented by a collection of simple subdomains called finite elements. The collection of these finite elements is called the finite element mesh.
2. Over each finite element, the physical process or governing equation is approximated by functions of a desired type (polynomials or otherwise), and algebraic expressions relating physical quantities at selective points, called nodes, of the element are developed.

3. The resulting element equations are assembled using continuity and/or a balance of physical quantities and solved.

The accuracy of the finite element solution depends on the element dimension analyzed, the order of the approximation function used, the shape of the element and the refinement of the mesh.

2.2.2 Element Dimension

One-dimensional finite element models are represented by ordinary differential equations and developed based on the assumption that the physical process is significant in only one direction. Some examples of 1-D problems include conduction heat transfer in a plane wall or fin, axial deformation of a bar or flow through channels and pipes. In each of these problems, the unknown solution, U, (temperature, displacement or velocity) is a function of only one variable (i.e., U(x)).

Two-dimensional finite element models are represented by partial differential equations and developed assuming the physical process is significant in two directions. These problems include conduction heat transfer in a long, prismatic solid, transverse deflection of a thin elastic membrane or 2-D rotational flow of a fluid. In these problems, U is a function of two variables (i.e., U(x,y)). Three-dimensional models are also represented by partial differential equations but are based on physical processes, which vary significantly in three directions. Types of 3-D problems include heat transfer in a short rectangular parallelepiped, combined (axial, shear, bending and torsion) loading of an elastic member or 3-D rotational flow. In these problems, U is a function of three variables (i.e., U(x,y,z)).

2.2.3 Element Order

Element order refers to the degree of polynomial used to approximate the finite element solution. The approximation solution, u, must fulfill three requirements to ensure its convergence to the actual solution, U, as the finite element mesh is increased. These requirements are (Reddy 1993b; Zeid 1991):

1. the polynomial is continuous and differentiable over the element,
2. the polynomial is *complete*, i.e., includes all lower-order terms up to the highest order used and
3. the polynomial is an interpolant of the primary unknowns (i.e. displacements, temperatures, velocities, etc.) at the nodes of the element.

The reason for the first requirement is it ensures that the polynomial contains nonzero coefficients. The second requirement is necessary in order to capture all possible states, i.e., constant, linear and so on, of the actual solution. For example, if a linear polynomial without the constant term is used to approximate the displacement of an axially loaded bar (a one-dimensional system), the approximate solution would never be able to represent a constant displacement in the element. The third requirement is necessary in order to satisfy the essential boundary conditions of the element and enforce continuity of the primary unknowns at points common to several elements.

2.2.4 Element Shape

The shape of the elements used to represent the domain of a problem is such that the approximation functions can be uniquely derived. Most finite elements are geometrically simple enough to meet this requirement. The shapes of one-dimensional elements are

line segments, as shown in Figure 2.2a. These elements have two to four nodes (depending on the approximation polynomial used) with one, two or more degrees of freedom per node.

Figure 2.2b shows common two-dimensional elements. Historically, triangular elements were developed first because they were easy to develop and formulate by hand (Zeid 1991). The three-node (linear) triangular element is the simplest 2-D element. The ten-node (cubic) triangular element has nine nodes on its boundary and one node inside the boundary.

Three-dimensional elements (Fig. 2.2c) are usually 3-D counterparts of 2-D elements. For example, the 4-node (linear) tetrahedral element is comprised of four linear triangular (2-D) elements. Creating 3-D finite element meshes is usually labor-intensive and an error-prone process. Thus, using automatic mesh generation algorithms in FEA packages can be beneficial in discretizing 3-D objects (Zeid 1991).

2.2.5 Mesh Refinement

Mesh refinement involves several options. Subdividing existing elements into a higher number of elements of the same order can refine the mesh. This is called *h-version mesh refinement* (Reddy 1993c). Alternatively, existing elements can be replaced by elements of higher order. This is called *p-version mesh refinement* (Reddy 1993c). In any given problem, one begins with a finite element mesh that is believed to be adequate to solve the problem at hand. Then as a second choice, another mesh is selected that consists of either a larger number of or higher order elements to solve the problem once again. If

facing page 12

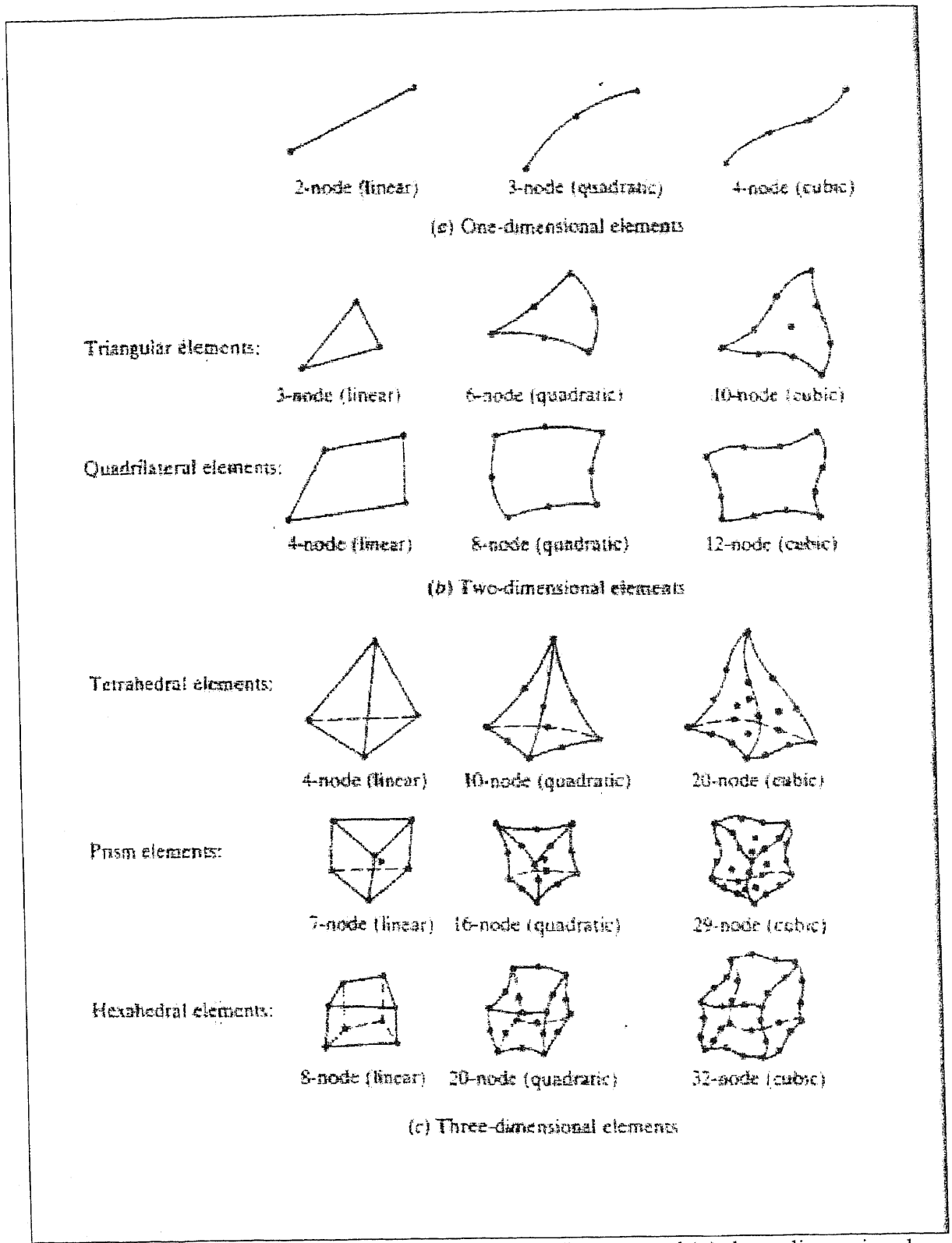

Figure 2.2 Types, shapes and orders for (a) one-, (b) two- and (c) three-dimensional elements.

Source: I. Zeid. 1991. "Finite Element Analysis." in *CAD/CAM Theory and Practice*. ed. J. J. Corrigan and J. M. Morriss. New York: McGraw-Hill, Inc. pp. 881-918.

there is a significant difference between the two solutions, further refinement is needed. If the difference is negligibly small, further refinements are not necessary.

2.3 Load Representation of the Hip

A suitable orientation of the hip must be selected in order to best simulate the loading conditions of the femur. Several force determination studies have been performed in an attempt to determine the magnitudes and directions of joint reaction and muscle forces acting at the hip. Static (McLeish & Charnley 1970), dynamic (Paul 1976), in-vitro (Merchant 1966), in-vivo (Davy et al. 1988; Hodge 1989; Breeman et al. 1993) and mathematical modeling (Crowninshield and Brand 1981) analyses have been implemented to determine the joint reaction and muscle forces exerted at the hip.

2.3.1 Joint Loading

The static analysis of McLeish and Charnley (1970) involved the use of a two-dimensional model to determine joint reaction forces. The load simulation used in the analysis represented the stance phase of slow walking elderly patients. Joint reaction forces of 2 to 3 times the body weight were determined in the coronal plane of the femur.

The dynamic analysis of Paul (1976) on joint reaction forces transmitted to the human body has been accepted as representative of hip forces during walking. Two peaks of joint loading were observed. The first peak corresponded to the early stance or "heel strike" position at 7% of the walking cycle. The second corresponded to the late stance or "toe off" position at 47% of the cycle. The joint load magnitudes determined from this study were 4 to 5 times body weight. The directions of the maximum joint load at "heel

strike" and "toe off" of the walking cycle reflect the three-dimensional loading nature of the joint reaction with components in both the coronal and sagittal planes.

In-vivo measurements of forces acting on hip implants have been performed using telemetry methods (Davy et al. 1988; Breeman et al. 1993) and an implant instrumented with pressure transducers measuring contact pressure between the implant head and the pelvic acetabulum (Hodge et al. 1989). The findings of these investigations correspond to the directions of the joint load as defined by Paul (1976) reflecting the three-dimensional nature of the load. However, the magnitudes of these loads are nearer to those defined in McLeish and Charnley (1970) at 2 to 3 times the body weight.

2.3.2 Muscle Loading

In order to represent a physiological distribution of bone strain in-vivo, muscle forces must be simulated in order to balance the reactions induced by the joints and thus stabilize the hip. In most force determination studies, it is often necessary to assume that each muscle group has a single resultant force (Paul 1976) in order to reduce the complexity of the study. The static investigation of McLeish and Charnley (1970) examined particular muscle groups in isolation and determined muscle forces under the assumption that these muscles acted alone. Their study of abduction forces in the one-legged stance predicted abductor muscle loads of 66% of the joint reaction force.

Merchant's (1966) in-vitro study of hip abductor muscle forces included the use of a skeletal model and springs to simulate the abductor muscles. Weights were hung at the center of gravity of the pelvis and the corresponding spring forces required to resist the

load were recorded. Results of this investigation predicted abductor muscle forces of 63% of the joint reaction.

Mathematical modeling has also been used to determine the load carried by various muscles. Optimization criteria have been employed to determine joint loads in a manner similar to dynamic analyses. In order to achieve more physiological data, others have used a muscle stress/endurance relationship as an optimization criterion (Crowninshield and Brand 1981). Results from this study predict values for the abductor muscles of 62% of joint reaction, which is in agreement with the results of MeLeish and Charnley (1970) and Merchant (1966).

2.4 Material Properties

In order to obtain optimal artificial hip performance it is imperative for one to select appropriate materials. The selection of implant materials is based on several characteristics, which include physical metallurgy, biocompatibility and mechanical performance. Physical metallurgy deals with the process involved in material enhancement through variations in its chemical composition (Holtzclaw et al. 1991). Biocompatibility is the ability of a material to perform with an appropriate host response in a specific application (Ratner et al. 1996a). All materials have imposed upon them mechanical requirements that originate from their physical properties (Ratner et al. 1996a). Properties such as ultimate strength, yield strength, fatigue strength and modulus of elasticity provide important information about the mechanical performance of a material.

2.4.1 Titanium

Rapid and significant progress has been made in the development of orthopaedic implants. As material requirements have become increasingly sophisticated, titanium and its alloys have been examined within numerous hip implant studies. Of the many titanium alloys that have been found to be suitable for orthopaedic applications, commercially pure (CP) titanium (ASTM F67) and titanium-aluminum-vanadium (Ti-6Al-4V) alloy (ASTM F136) are commonly used (Ratner et al. 1996b).

The term commercially pure (CP) titanium is applied to unalloyed titanium and designates several grades containing minor amounts of impurity elements such as carbon, iron and oxygen (Winter et al. 1980c). The microstructure of CP titanium is alpha hexagonal-close-packed (HCP) with relatively low strength and high ductility (Winter et al. 1980c). The amount of oxygen can be controlled at various levels to provide increased strength (Ratner et al. 1996b). Moreover, the material may be slightly cold worked for additional strength.

The addition of aluminum to titanium stabilizes the alpha structure, while vanadium addition produces and stabilizes its beta body-centered-cubic (BCC) structure (Winter et al. 1980c). For orthopaedic applications where high strength and fatigue resistance is required, the material is annealed (Ratner et al. 1996b). The annealed microstructure corresponds to a uniform distribution of the alpha and beta structures.

The biocompatibility of titanium based materials is recognized by several medical researchers. Titanium appears to have an extremely low toxicity and is well tolerated by tissue (Meachim and Williams 1973). Some patients may be allergic to metals in contact with their skin. Similarly, allergic reactions of various severity are known to occur with

implant materials, and in some cases, eczematous dermatitis related to internal exposure are known to occur (Winter et al. 1980c). Titanium does not cause any sensitivity, nor do any of the alloying elements in Ti-6Al-4V (Williams 1977).

The mechanical properties of commercially pure (CP) titanium (F67) and Ti-6Al-4V alloy (F136) are listed in Table 2.1. The yield strength of heat-treated F136 is more than twice that of F67. The elastic modulus of titanium alloys is low in comparison with other implantable metals (Winter et al. 1980c; Ratner et al. 1996b). A material with a low modulus is less rigid and deforms elastically under applied loads. This property plays a significant role in the development of orthopaedic implants where a close match is desired between the elastic properties of bone and the implant. The fatigue strength of F136 is more than twice that of F67. Stress raisers, such as sharp corners, notches, and holes decrease the fatigue properties (Winter et al. 1980c). This is one of the reasons why these geometrical features are usually avoided in design and manufacturing.

Table 2.1 Typical mechanical properties of surgical titanium alloys.

ASTM Designation	**Condition**	**Young's Modulus (GPa)**	**Yield Strength (MPa)**	**Tensile Strength (MPa)**	**Fatigue Strength (at 10^7 cycles) (MPa)**
F67	30% Cold worked Grade 4	110	485	760	300
F136	Forged annealed	116	896	965	620
	Forged, heat treated	116	1034	1103	620-689

Source: B. D. Ratner, A. S. Hoffman, F. J. Schoen, and J. E. Lemons. 1996. "Classes of Materials Used in Medicine." in *Biomaterials Science: An Introduction to Materials in Medicine.* New York: Academic Press. pp. 37-50.

2.4.2 Cobalt-Chromium

Within the overall classification of cobalt-chromium alloys, there are four that are currently used for surgical applications, which include ASTM F-75, F-90, F799 and F-562 (Ratner et al. 1996b). For most cable designs, the ASTM F-90 alloy has been found to be satisfactory, combining good mechanical properties with admirable corrosion resistance and machinability (Winter et al. 1980a).

The F-90 alloy is a Co-Cr-W-Ni alloy (Ratner et al. 1996b). Its crystal structure is comprised of both hexagonal-close-packed (HCP) and face-centered-cubic (FCC). The HCP structure is promoted by additions of chromium and tungsten while the FCC phase is stabilized by nickel. The tungsten and nickel additions also improve machinability and fabrication properties (Ratner et al. 1996b).

In any surgical application, a number of different types of corrosion can occur, which include uniform, galvanic and crevice (Winter et al. 1980a). The overall level of corrosion from uniform surface attack on cobalt-chromium alloys is considered to be minimal with only marginal differences being found between the various types (Kuhn 1981). The coupling of cobalt-chromium alloy components with those of other alloys is usually avoided for fear of galvanic corrosion (Winter et al. 1980a). However, for cobalt-chromium alloys, this danger is less pronounced even when they are coupled with carbon or titanium, both of which are cathodic to them, no galvanic corrosion effects have been observed (Acharya et al. 1970).

Crevice corrosion is the principal form of corrosion observed around multicomponent surgical implants and is found when two or more components meet to form an interface (Winter et al. 1980a). Due to the frequency with which such corrosion is encountered, a

great deal of research has been conducted in this area and is generally agreed that the F-75 cobalt-chromium alloy exhibits the highest crevice corrosion resistance followed in order by F-90 and F-562 (Devine and Wulff 1976).

There is some evidence that even the corrosion-resistant cobalt-chromium alloys produce some minute quantities of corrosion products that may be responsible for metal sensitivity in patients (Evans et al. 1974). Surgical removal of the device eliminates the symptoms, thus establishing a clear cause and effect. All sensitivity cases reported involve stainless steel or cobalt-chromium alloys, which would indicate that the common elements in these alloys might be the sensitizing constituents (Evans et al. 1974).

The mechanical properties of the cobalt-chromium alloys resulting from various processes are listed in Table 2.2. In the annealed state, the mechanical properties of F90 approximate those of F75 alloy, but when cold worked, the properties double.

Table 2.2 Typical mechanical properties of surgical cobalt-chromium alloys.

ASTM Designation	Condition	Young's Modulus (GPa)	Yield Strength (MPa)	Tensile Strength (MPa)	Fatigue Strength (at 107 cycles) (MPa)
F75	As-cast/annealed	210	448-517	655-889	207-310
F799	Hot forged	210	896-1200	1399-1586	600-896
F90	Annealed	210	448-648	951-1220	Not available
	44% Cold worked	210	1606	1896	586
F562	Hot forged	232	965-1000	1206	500
	Forged, heat treated	232	1500	1795	689-793

Source: B. D. Ratner, A. S. Hoffman, F. J. Schoen, and J. E. Lemons. 1996. "Classes of Materials Used in Medicine." in *Biomaterials Science: An Introduction to Materials in Medicine.* New York: Academic Press. pp. 37-50.

CHAPTER 3

MATERIALS AND METHODS

3.1 Solid Model Development

The first phase of the investigation is to develop a three-dimensional solid model of the geometry of the critical section of each femoral implant. The critical section is defined near the proximal end of the stem around the hole where the cables of the cable grip system are threaded. Two solid models are created using Pro/Engineer (Version 19). One consists of the critical section with a plug in the hole and the other consists of the critical section without the plug.

Figure 3.1 illustrates the solid model of the critical section of the non-plugged implant. The transverse view (Fig. 3.1b) shows the cross-section geometry of the model. In reviewing the literature for stem cross-section geometry, the shape in Figure 3.1b represents a suitable geometry for stem cross-sections designed to minimize cement stresses (Crowninshield et al. 1980).

Figures 3.1c and 3.1d illustrate the coronal and sagittal views of the critical section of the non-plugged model. As the Figures show, the model has straight contours. As discussed in Tarr's (1982) research on total hip femoral design, straight stem implant design is becoming more common because such implants are neutrally oriented and easily inserted or removed during surgery. Moreover, for cement applications, such contours reduce the possibility of air pocket development at the implant-cement interface by allowing a complete covering of cement around the stem.

On the inside of the hole (Fig. 3.1c), two cylinders are used to represent the geometry of the cables (from the attached cable grip system) that are in contact with the implant.

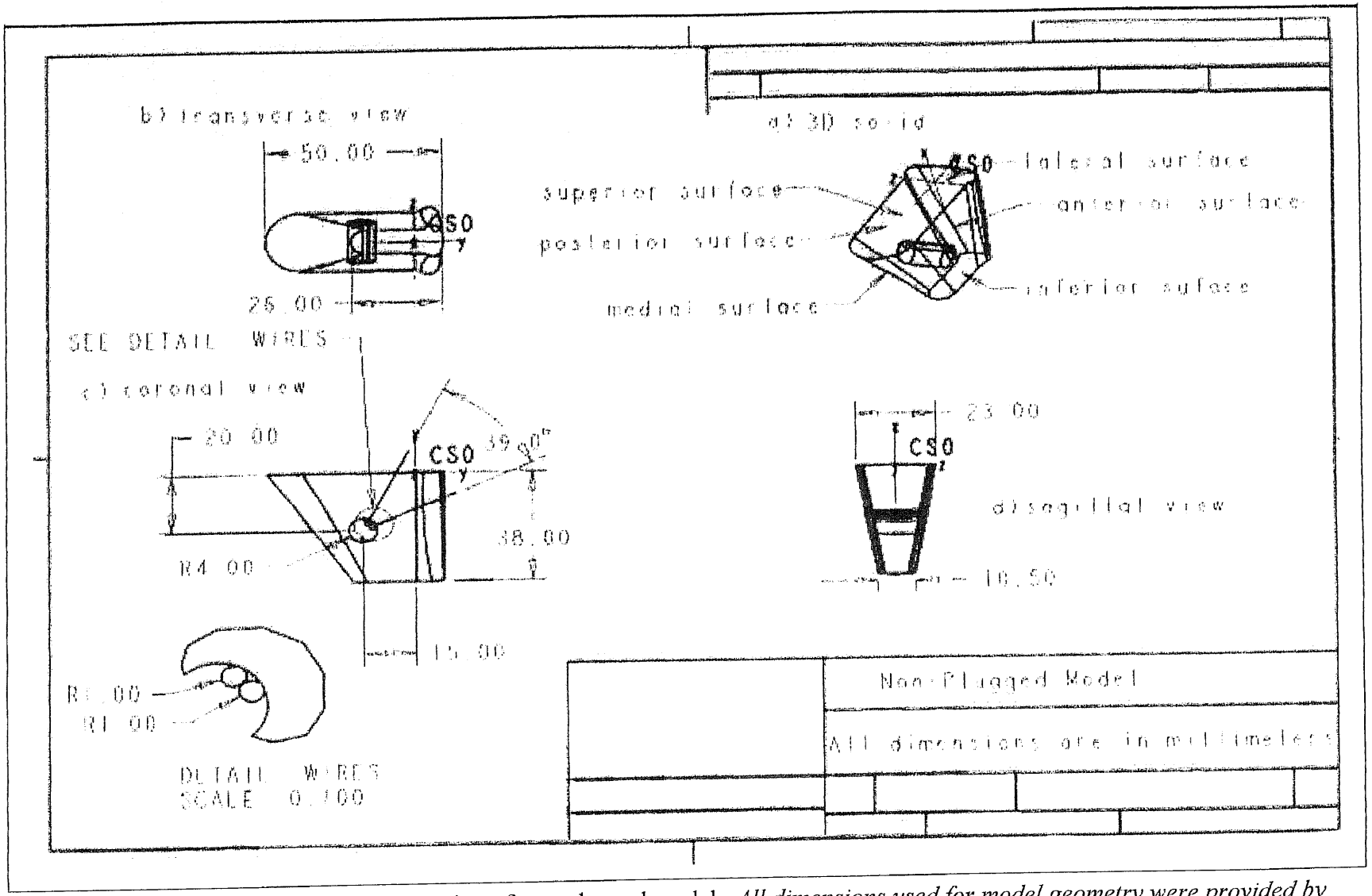

Figure 3.1 Solid model of critical section of non-plugged model. *All dimensions used for model geometry were provided by Howmedica Inc.*

The 39° position of the cables (information provided by Howmedica Inc.) represents a case where the cables are close to each other inside of the hole, but do not overlap.

Figure 3.2 shows the solid model of the critical section of the plugged implant stem. The geometry of the plugged model is similar to that of the non-plugged with one exception. As illustrated in the coronal view (Fig. 3.2a), the hole in the implant stem of the plugged model is enlarged to a diameter equal to the outer diameter of the plug. This equality in diameters is used in order to represent perfect contact (without gaps or interference) between the plug and the implant. The inner diameter of the plug in the plugged model is equal to the diameter of the hole in the non-plugged model (Refer to the numerical data in Figures 3.1c and 3.2a). The cables in the plugged model are created in the same way as those in the non-plugged model (Refer to the numerical data in Figures 3.1c and 3.2a).

3.1.1 Element Representation for Initial Mesh

Each model is divided into a number of finite elements. The collection of these elements produces an initial mesh of each model. The purpose of meshing is to approximate a stress solution for each element in order to represent the solution over the entire model.

ANSYS (Version 5.4) is used to develop the initial mesh of each model geometry (with and without the plug). Since the geometry is created using Pro/Engineer, three-dimensional meshing of the geometry is limited to tetrahedral elements. This limitation results from the conversion of Pro/Engineer files to ANSYS files. For this reason, first order (4 node) tetrahedral elements are used to mesh the solid models of the implant and the plug. The cables are meshed using first order (2-node) truss elements. Each element

facing page 21

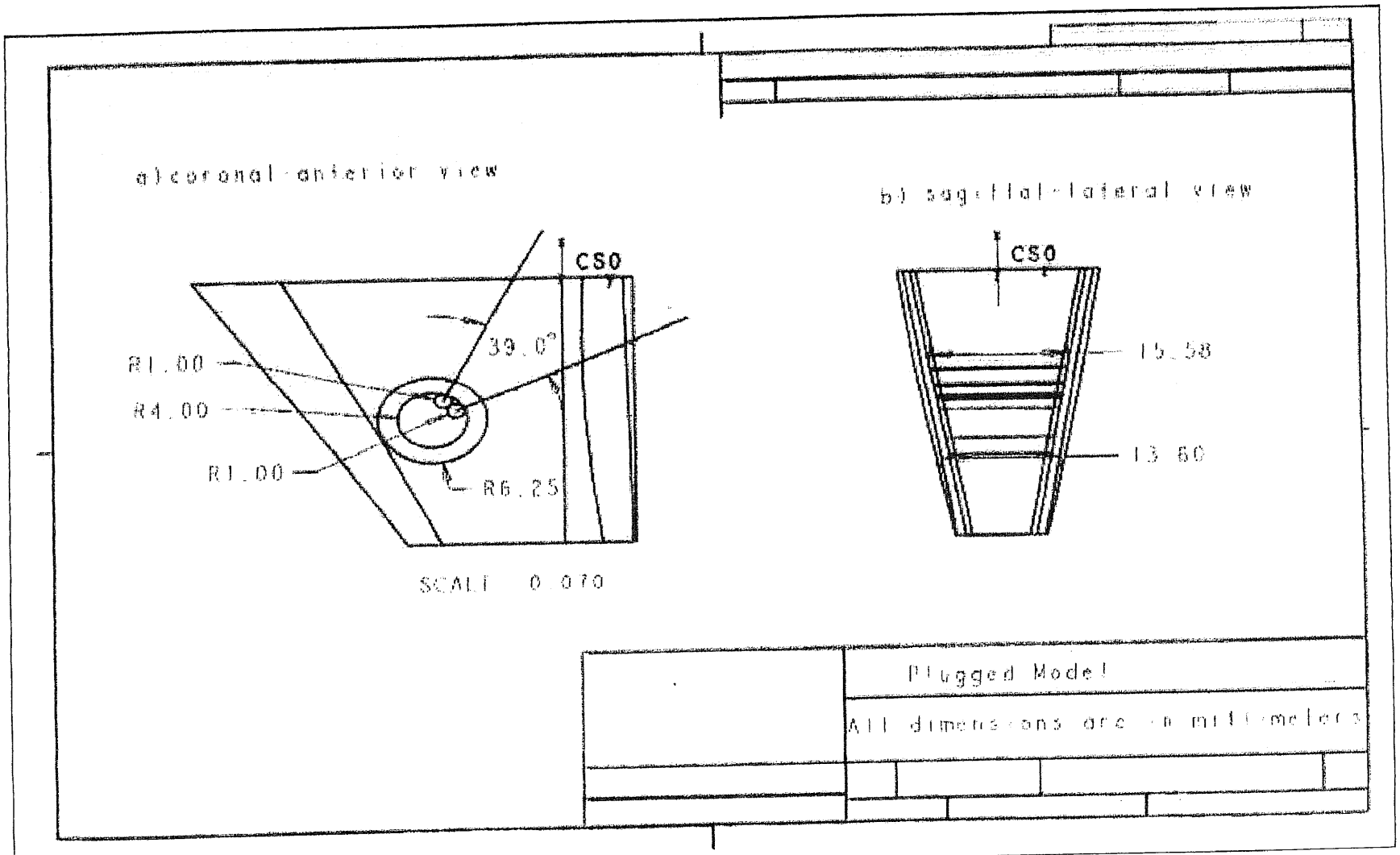

Figure 3.2 Solid model of critical section of plugged model. *All dimensions used for model geometry are provided by Howmedica Inc.*

has six degrees of freedom per node which allows translation and rotation in the x (superior-inferior), y (medial-lateral) and z (posterior-anterior) directions. The initial mesh for the plugged model contained 107 elements and 32 nodes. For the non-plugged model, the initial mesh contained 100 elements and 27 nodes.

3.1.2 Constraints

The inferior surface (Fig. 3.1a) of each model is constrained to prevent movement in the x (superior-inferior), y (medial-lateral) and z (posterior-anterior) directions. These constraints represent a cementless fixation of the implant stem within the canal of the femur. There are two types of cementless fixations (Walker and Robertson 1988) which include the "press fit" stem and the "coated" stem. A "press fit" stem is one where the implant is made slightly larger than the femur's canal. The interference between the stem and the bone provides the stability. In a "coated" stem, a three-dimensional coating is applied to the implant. The bone in contact with the coating grows into it and anchors the implant. Since there is only a slight difference between the conditions of "press-fit" and coated" stems, the constraint simulation in the current study can be applied to either of the two conditions.

The plane of symmetry for each model is constrained in the z (posterior-anterior) direction. Since each model simulates the initial use in post-surgery of the implant, it is assumed that the cables of the cable grip system do not slide during this period. For this reason, additional rotational constraints are applied to the cables in each model.

3.1.3 Material Properties

The material properties required for the analysis are the modulus of elasticity, Poisson's ratio and density for the implant, the cables and the plug. Table 3.1 lists the material properties used in the analysis for each component (Ratner et al. 1996b; Hibbeler 1994a; Halliday and Resnick 1988). All materials are assumed to be linear and isotropic (Ugural and Fenster 1995b). For the implant, the titanium-aluminum-vanadium (Ti-6Al-4V) alloy ASTM F136 is used as the material. According to the literature, Ti-6Al-4V is considered to be a suitable material for femoral implants due to its close match of elastic properties with bone (Winter et al. 1980c; Tarr 1982), low toxicity (Williams 1977) and its good tissue tolerance (Meachim and Williams 1973). The modulus, Poisson's ratio and density of Ti-6Al-4V are 116 GPa (16.82 Mpsi), 0.36 and 4510 kg/m^3 (281.56 lb/ft^3) respectively (Table 3.1).

For the cables, the cobalt-chromium (Co-Cr-W-Ni) alloy ASTM F90 is used. According to the literature, the F90 is commonly used in the design of cables due to its good mechanical properties (Winter et al. 1980a), notable machinability and fabrication (Ratner et al. 1996b) and high corrosion resistance (Kuhn 1981; Acharya et al. 1970). The modulus, Poisson's ratio and density of Co-Cr-W-Ni are 210 GPa (30.45 Mpsi), 0.3 and 8850 kg/m^3 (552.51 lb/ft^3) respectively. For the material of the plug, the F90 alloy is also used to allow a matching of materials between the cables and the plug.

Table 3.1 Material properties for model components.

Component	Density[a] (kg/m^3)	Young's Modulus[b] (GPa)	Poisson's Ratio[c]
Implant	4510	116	0.36
Cables	8850	210	0.3
Plug	8850	210	0.3

[a]Halliday and Resnick 1988 [b]Ratner et al. 1996b [c]Hibbeler 1994a

3.1.4 Load Conditions

3.1.4.1 Cable Load: During each simulation, a tensile force of 223 N (50 lb) is applied along the cables. This force represents a pre-tensioned condition of the cables after the Dall-Miles Cable Grip System is applied to the implant (information provided by Howmedica Inc.). As the cables are pulled on the anterior and posterior planes of the implant, the tensile force becomes a contact force. This force is applied (parallel to the anterior and posterior planes along the direction of the cables) to small areas inside of the hole where the cables are in contact with the implant (Fig. 3.3). The x and y components of the contact force (Table 3.2) are determined based on the angular position of the cables (Fig. 3.3) in the coronal plane (Refer to Appendix A for a detailed calculation of cable contact force components).

Since it is assumed that the cables are not pulled in a direction perpendicular to the coronal plane of the implant (away from the hole), the contact force angle, θ_{xz}, as well as the z component of the contact force, $F_{zcontact}$, in the sagittal plane is equal to zero.

Table 3.2 Magnitudes of contact force components applied to the implant by the cables inside of the hole (Refer to Appendix A for calculation of cable force data).

	Cable 1	**Cable 2**
Contact Force Angle θ_{xy} (°)	25.5	64.5
$F_{contact}$ (N)	223	223
$F_{xcontact}$ (N)	-96.0	-201.2
$F_{ycontact}$ (N)	201.2	96.0
$F_{zcontact}$ (N)	0	0

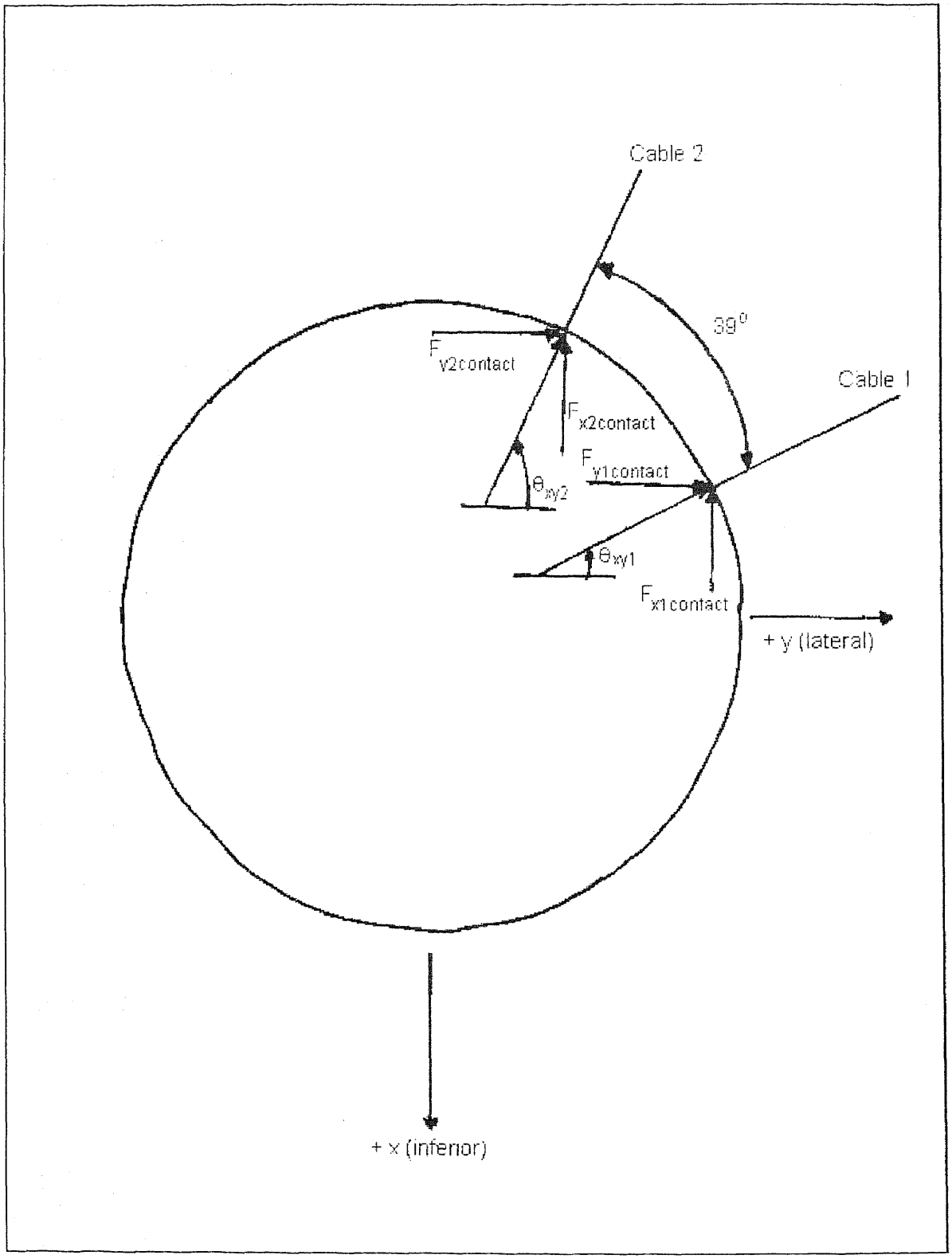

Figure 3.3 Schematic of contact force application inside of the hole (coronal plane view).

3.1.4.2 Implant Load: According to the literature (Breeman et al. 1993), there are two instances during a walking cycle (Figure 3.4) where the hip is exposed to maximum joint reaction and abductor muscle forces. These instances correspond to the early stance or full "heel strike" position ("1. Max" in Fig. 3.4) and the late stance or full "toe off" position ("2. Max" in Fig. 3.4).

The load conditions applied to both the plugged and non-plugged models of the implant stem are based on conditions at the full "heel strike" (HS) position of a normal walking cycle (1. Max in Fig. 3.4). Figure 3.5 provides a schematic of an implanted femur indicating the joint reaction and abductor muscle forces exerted on the left hip at the full HS position. The magnitudes of these forces (Table 3.3) were provided by Howmedica Incorporated, which were determined with the femur oriented in 9° of adduction and 27° of flexion (Refer to Appendix B for further explanation of the joint reaction and muscle forces applied to the femur at full "heel strike").

Table 3.3 Joint reaction and abductor muscle forces exerted on the hip at full "heel strike" position of a normal walking cycle. *Information provided by Howmedica Inc.*

	F^{b}_{joint}	F^{c}_{muscle}
$F^{a}_{resultant}$ (N)	2386.4	1102.2
F_x (N)	2195	-975.1
F_y (N)	755.7	-479.1
F_z (N)	-552.9	301.1

[a]Loads are based on an average body weight of 700.2 N (157.4 lb).
[b]Joint resultant load represents 3.4 times the average body weight.
[c]Muscle load represents the summation of the muscle forces generated by the gluteus medius and minimus.

facing page 25

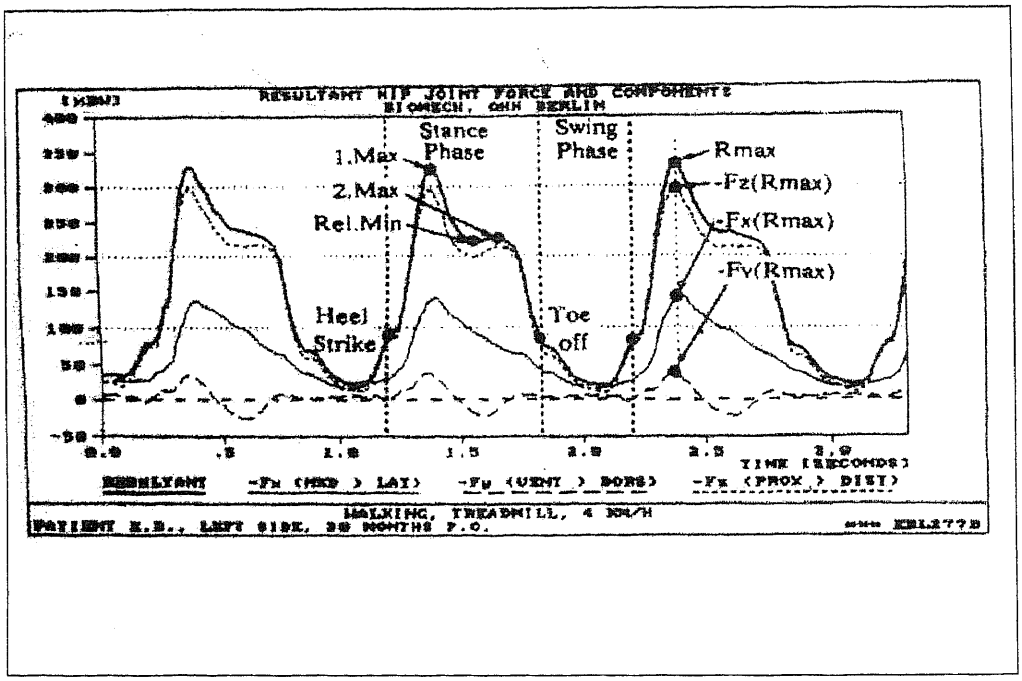

Figure 3.4 Hip joint forces exerted on an implanted left femur of an elderly patient during normal walking.
Source: G. Breeman, F. Graichen, and A. Rohlmann. 1993. "Hip Joint Loading During Walking and Running, Measured in Two Patients." *J. of Biomech.* 26:969-990.

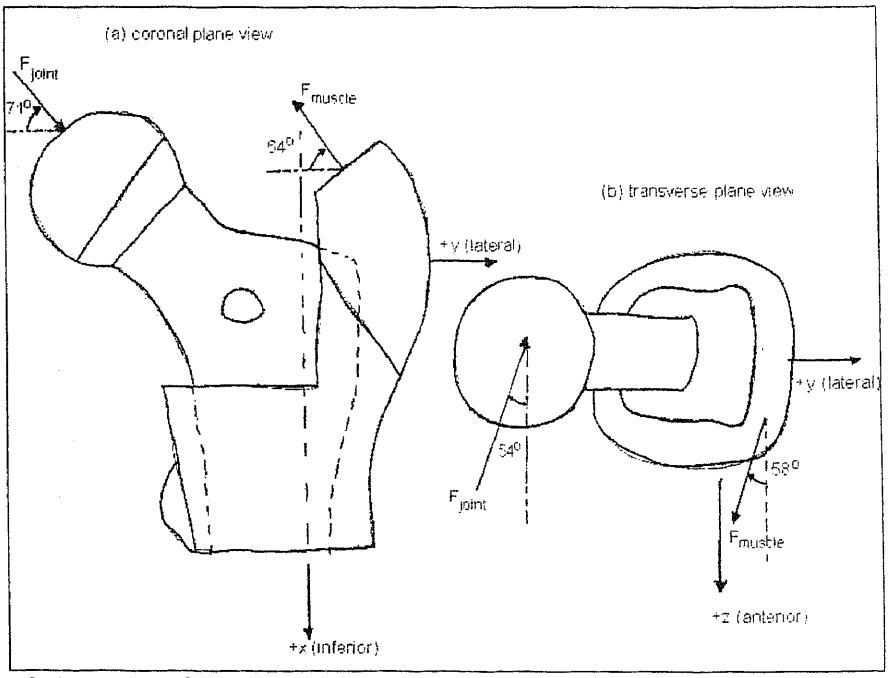

Figure 3.5 Schematic of left implanted femur indicating joint reaction and muscle forces in the (a) coronal plane and (b) transverse plane views.

3.2 Simulation Conditions

3.2.1 Static Case

A static simulation is performed on each model in the analysis, which represents the instant in a normal walking cycle that a hip is subjected to full "heel strike" (HS) loading conditions. This position of the stance phase is an ideal choice for the static simulation because the loads exerted on the hip are highest at this point in the cycle ("1. Max" in Fig. 3.4). During this simulation, only external loading of the hip (joint reaction and abductor muscle forces) is considered in order to determine the effect of the plug on the *static* performance of the implant.

In order to obtain the stress distribution within the critical section of the implant, the joint reaction and abductor muscle forces (Fig. 3.5) are transferred to the superior surface of each model (Fig. 3.6) using basic static equilibrium equations (Meriam and Kraige 1992a). As the joint reaction and abductor muscle forces are transferred, moments are produced. In the coronal plane (Fig. 3.6a), the x (superior-inferior) and y (medial-lateral) components of the joint reaction and muscle forces produce the axial and shear forces, F_{xmodel} and F_{ymodel}, as well as a bending moment, M_{zmodel}, about the z (posterior-anterior)-axis on the superior surface of the model. These forces are uniformly distributed on the superior surface.

In the transverse plane (Fig. 3.6b), the z component of the joint reaction and muscle forces produce a shear force, F_{zmodel}, as well as a bending moment, M_{ymodel}, about the y-axis and a torsional moment, T_{xmodel}, about the x-axis. These forces are also uniformly distributed on the superior surface. Table 3.4 provides a sum of the magnitudes of the forces and moments applied to the superior surface of each model resulting from the load

facing page 26

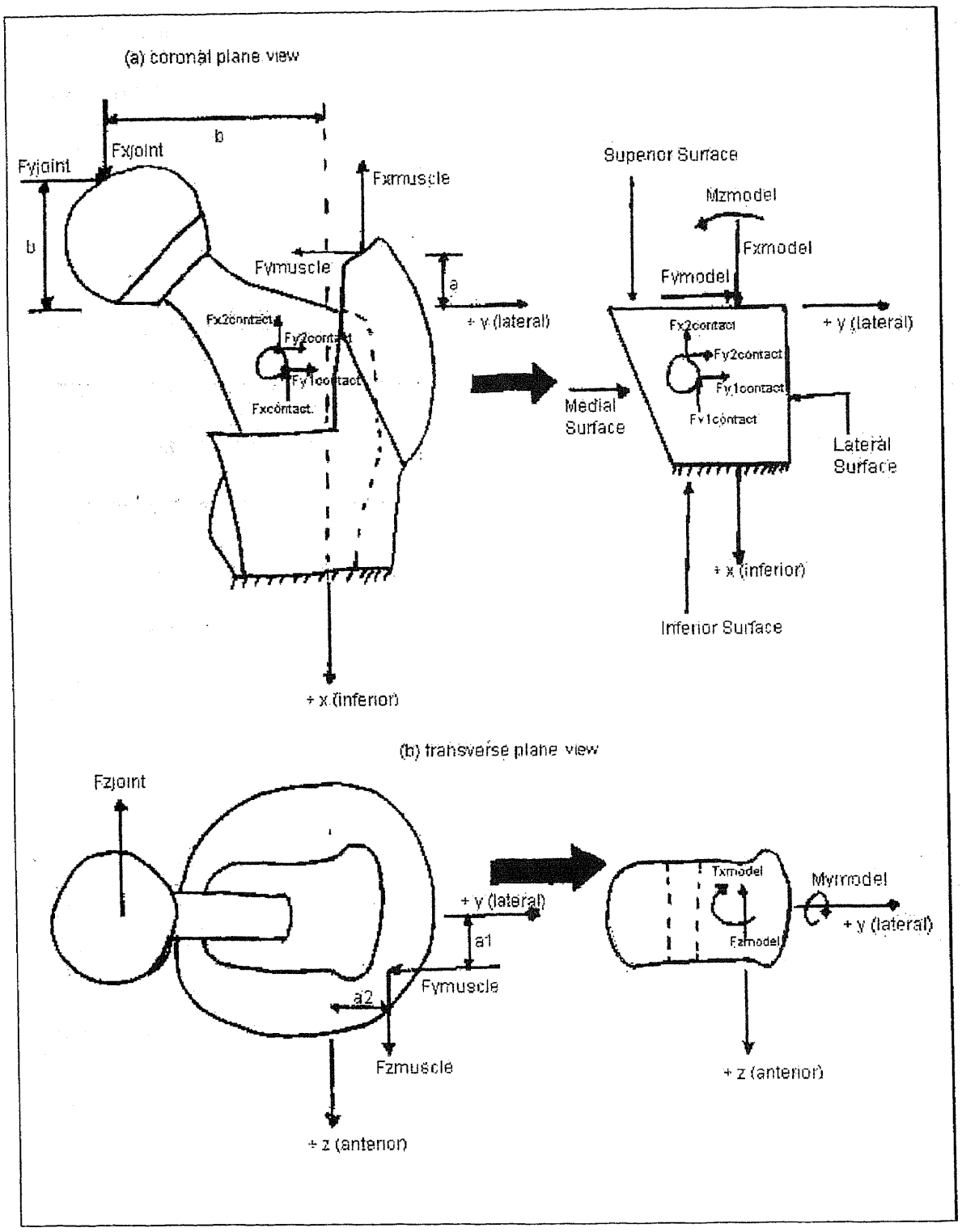

Figure 3.6 Schematic of load transformation to the superior surface of the model in the (a) coronal plane and (b) transverse plane views.

transformation (Refer to Appendix A for a detailed calculation of loads applied to the superior surface).

Table 3.4 Magnitudes of forces and moments applied to the superior surface of each model (Refer to Appendix A for detailed calculation of forces and moments).

	x component	y component	z component	Resultant
Force (N)	1220	276.6	-251.8	1276.1
Moment (N-m)	34.3	-15.2	114.1	120.11

3.2.2 Quasi-Dynamic Case

The stance phase of a normal walking cycle (Fig. 3.4) is divided into four sub-phases, which are defined as "heel strike" (HS), transition (TR), "foot flat" (FF) and "toe off" (TO). However, only the HS and FF sub-phases are used in the quasi-dynamic simulations. The time aspect of this simulation is based on results obtained from Breeman et al. (1993) study of hip joint loading during walking and running (Fig. 3.4). In this study, hip joint forces were measured on two patients using telemetry methods. The first patient was an elderly male who underwent bilateral joint replacement. The second was a female who received one instrumented hip implant in the right hip. The joint loading was observed over the first 30 and 18 months, for the male and female patient respectively, following implantation. Measurements were obtained as each patient underwent walking, jogging and stumbling. The joint reaction force vs. time graph (Fig. 3.4) is the result of the measurements obtained from the left hip of the elderly male patient during normal walking at a constant speed of 4 km/h (3.65 ft/s). Using this

graph (Fig. 3.4) as a basis for the quasi-dynamic simulation, the stance phase is defined as the period from "heel strike" to "toe off" (Fig. 3.4), which is approximately 0.6 s.

The constant speed of 4 km/h (3.65 ft/s) is applied to each model throughout each sub-phase used in the quasi-dynamic simulation. The "heel strike" (HS) sub-phase (the first critical sub-phase of stance studied) is defined by the time interval $0 \text{ s} < t < 0.15$ s. This phase begins with minimum HS ("heel strike" in Fig. 3.4) at $t = 0$ s (where minimum loading is exerted on the hip) and ends with full HS ("1. Max" in Fig. 3.4) at $t = 0.15$ s (where absolute maximum loading is exerted). During this sub-phase, the joint reaction forces (as well as the muscle forces) increase linearly with time. For this reason, the loading is applied to the superior surface of each model in a *ramp* mode in order to best simulate the HS sub-phase of stance. In *ramp* mode, the loading conditions at minimum HS ($t = 0$ s) are applied to the model and increased linearly until absolute maximum loading conditions are applied at full HS ($t = 0.15$ s). For simplicity of the analysis, the loading conditions applied to the model at minimum HS, during HS ramp mode, are defined as zero. The loading conditions applied at full HS correspond to the absolute maximum loading conditions exerted on the hip. These conditions are defined by the same force (1276.1 N [286.87 lb]) and moment (120.11 N-m [88.59 lb-ft]) used in the static case (Table 3.4).

The transition (TR) sub-phase of stance is defined by the interval $0.15 \text{ s} < t < 0.225$ s. This phase begins with full HS ("1. Max" in Fig. 3.4) at $t = 0.15$ s (where absolute maximum loading is exerted on the hip) and ends with intermediate ("Rel. Min." in Fig. 3.4) "foot flat" (FF) at $t = 0.225$ s. (where intermediate loading is exerted). During this sub-phase, a transition from full HS to intermediate FF takes place resulting in a negative

linear variation in the loading exerted on the hip (Fig. 3.4). Since the load exerted on the hip during the TR sub-phase is lower than that exerted during HS, this sub-phase is not analyzed in the study.

The "foot flat" (FF) sub-phase (the last critical sub-phase of stance studied), is defined by the time interval $0.225 \text{ s} < t < 0.45 \text{ s}$. This phase begins with intermediate FF ("Rel. Min." in Fig. 3.4) at $t = 0.225$ s (where intermediate loading is exerted on the hip) and ends with full ("2. Max." in Fig. 3.4) "toe off" (TO) at $t = 0.45$ s. During this sub-phase (Fig. 3.4), the loading increases slightly from intermediate FF ($t = 0.225$ s, which is "Rel. Min." in Fig.3.4) to full TO at $t = 0.45$ s ("2. Max" in Fig. 3.4). Since the difference in magnitude between intermediate FF and full TO is small (less than 5%), the loading conditions at these points are assumed equal during the simulation. For this reason, the loading conditions are applied to the superior surface of each model in a *step* mode in order to best simulate the FF sub-phase of stance. In *step* mode, the intermediate loading conditions at intermediate FF ($t = 0.225$ s) are applied to the model and remain constant until full TO ($t = 0.45$ s) is reached.

The loading conditions applied to the model at intermediate FF, during step mode, is defined (using linear interpolation) as 60% of the absolute maximum conditions (Table 3.4) applied at full HS during HS ramp mode. The force (765.6 N [172.11 lb]) and moment (72.07 N-m [53.16 lb-ft]) applied to each model (which is also uniformly distributed across the superior surface) during the FF sub-phase of stance is summarized in Table 3.5.

Table 3.5 Magnitudes of forces and moments applied to the superior surface of each model during the "foot flat" sub-phase of stance.

	x component	y component	z component	Resultant
Force (N)	732	165.6	-151.1	765.6
Moment (N-m)	20.6	-9.1	68.5	72.07

The final sub-phase of stance, "toe off" (TO), is defined by the time interval $0.45 \text{ s} < t < 0.6 \text{ s}$. This phase begins with full TO ("2. Max." in Fig. 3.4) at $t = 0.45$ s and ends with minimum TO ("Toe Off" in Fig. 3.4) at $t = 0.6$ s. During this sub-phase, the joint reaction forces (as well as the muscle forces) decrease linearly with time. Since the load exerted on the hip during this sub-phase is lower than that exerted during FF, the TO sub-phase is not analyzed in the study.

3.3 Convergence Analysis for Final Mesh

The second phase of the analysis is to develop an optimal finite element mesh for each model using appropriate boundary conditions and performing a convergence analysis. Due to symmetry in geometry and loading about the median coronal plane, only half (posterior half) of each model is used for meshing. The final mesh is determined using the h-version mesh refinement method of convergence (Reddy 1993c). In this process, the initial mesh of the plugged (107 elements and 32 nodes) and non-plugged (100 elements and 27 nodes) models is used to obtain the first finite element solution. Increasing the number of the elements until the solution converges then refines the mesh. Convergence is reached when the difference between two consecutive solutions is within a specified tolerance. Each analysis is run with a tolerance set at 0.001.

Figure 3.7 shows a graph of the convergence analysis of each model (plugged and non-plugged) using the load conditions previously discussed (Section 3.1.4). The y-axis represents the finite element solution of the maximum von Mises stress (Ugural and Fenster 1995d) and the x-axis represents the iteration number corresponding to each mesh. For the plugged model (Fig. 3.7a), the solution converged at a mesh iteration number of 80 which corresponds to a total of 3969 elements and 1157 nodes. For the non-plugged model (Fig. 3.7b), the solution converged at a mesh iteration number of 65 which corresponds to 3085 elements and 841 nodes. Figure 3.8 shows the final finite element mesh of the plugged (Fig. 3.8a)and non-plugged (Fig. 3.8b) models respectively.

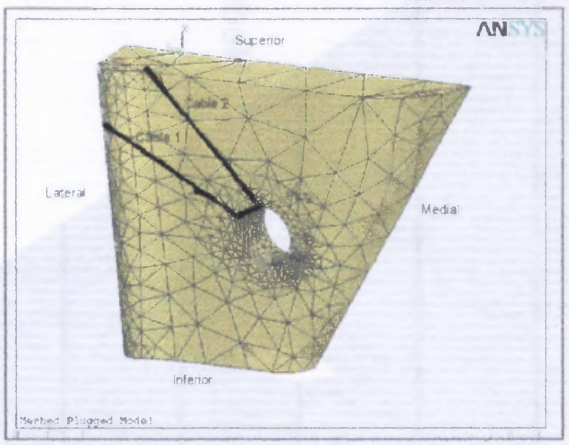

(a)

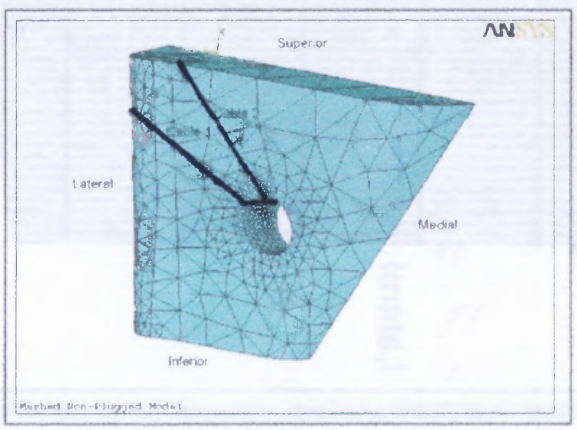

(b)

Figure 3.8 Final mesh of (a) plugged and (b) non-plugged models

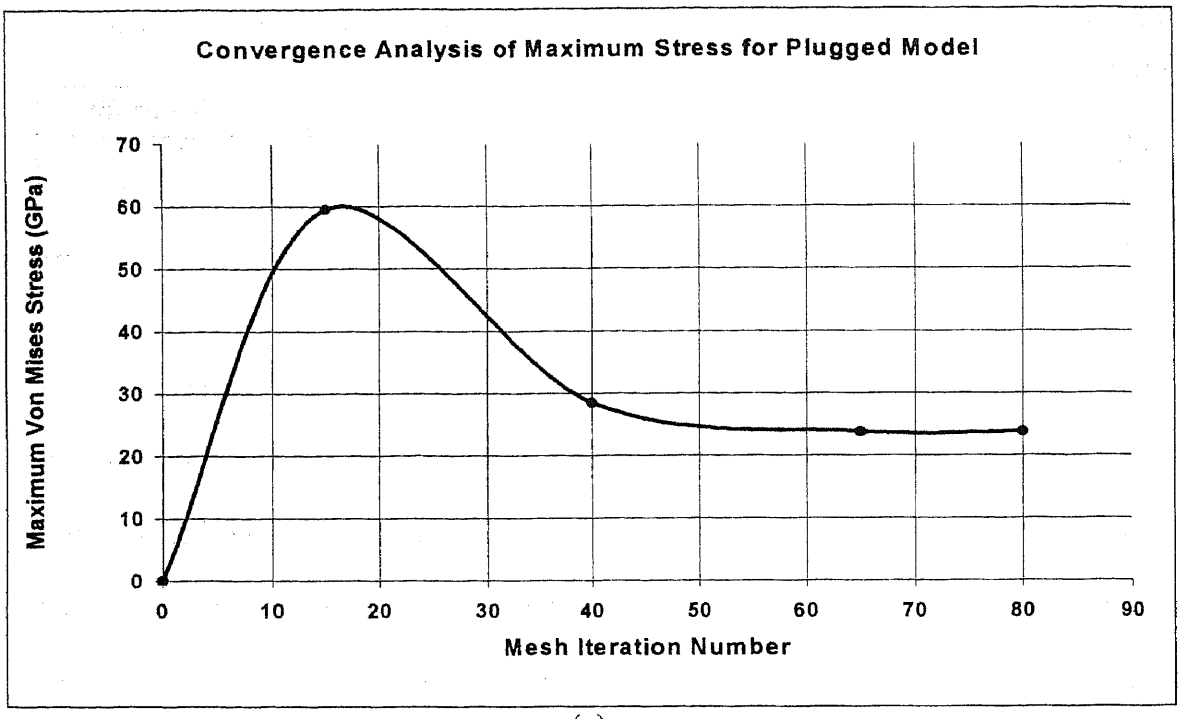

(a)

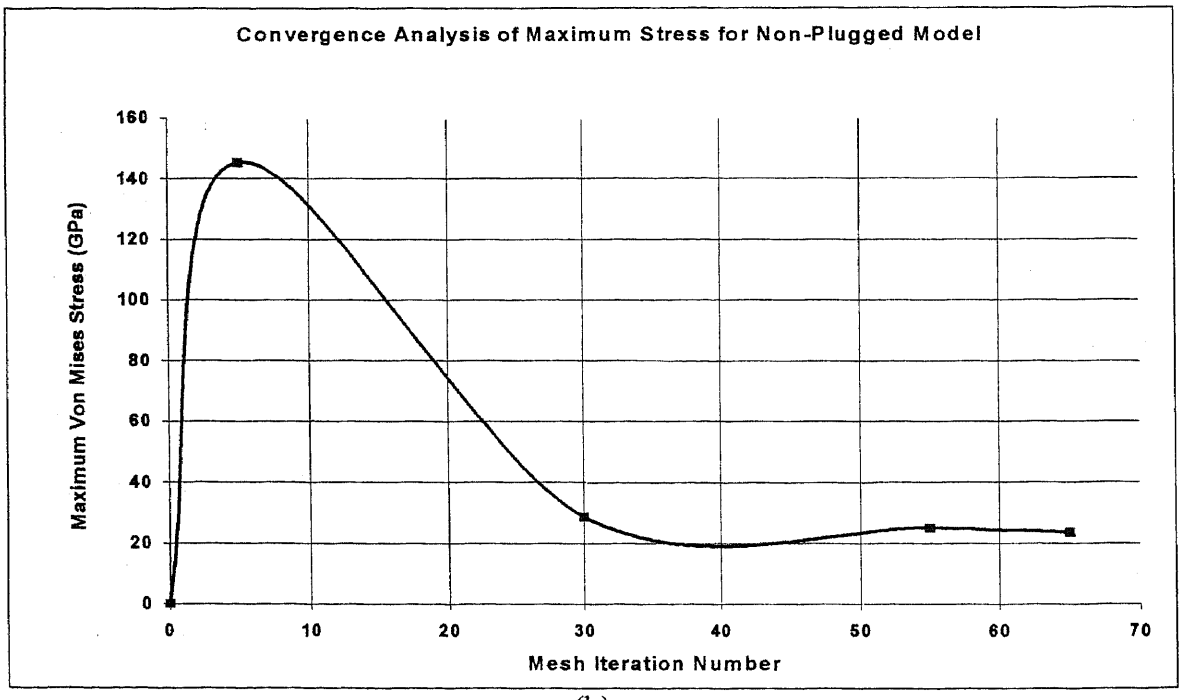

(b)

Figure 3.7 Convergence analysis for (a) plugged and (b) non-plugged models.

CHAPTER 4

RESULTS AND DISCUSSION

A Finite Element Analysis was performed to determine the effect of a cobalt-chromium plug on the performance of the critical section of a titanium alloy femoral implant coupled with a cobalt-chromium cable grip system. The critical section of the implant was defined near the proximal end of the stem around the hole where the cables were threaded. Two models were generated for the analysis. One consisted of the critical section with the plug in the hole (referred as "plugged" model) and the other was without the plug (referred as "non-plugged" model). Static and quasi-dynamic simulations were performed on each model. The static simulation represented the instant the hip is subjected to early stance or full "heel strike" loading conditions during normal walking. The quasi-dynamic simulation represented two sub-phases of stance (referred as "heel strike" and "foot flat") at a normal walking speed of 4 km/h (3.65 ft/s). The cables used in the simulations were pre-tensioned.

4.1 Results

4.1.1 Static Case

Figure 4.1 illustrates the FEA von Mises stress contours of the posterior side of the critical section of the non-plugged model. The minimum stress for the non-plugged model is located proximally at a point on the plane of symmetry between the superior and medial surfaces of the implant (node 176 in Fig. 4.1), which is away from the hole. The magnitude of the minimum stress is 30.343×10^{-3} GPa (4.399×10^{-3} Mpsi). The maximum

facing page 32

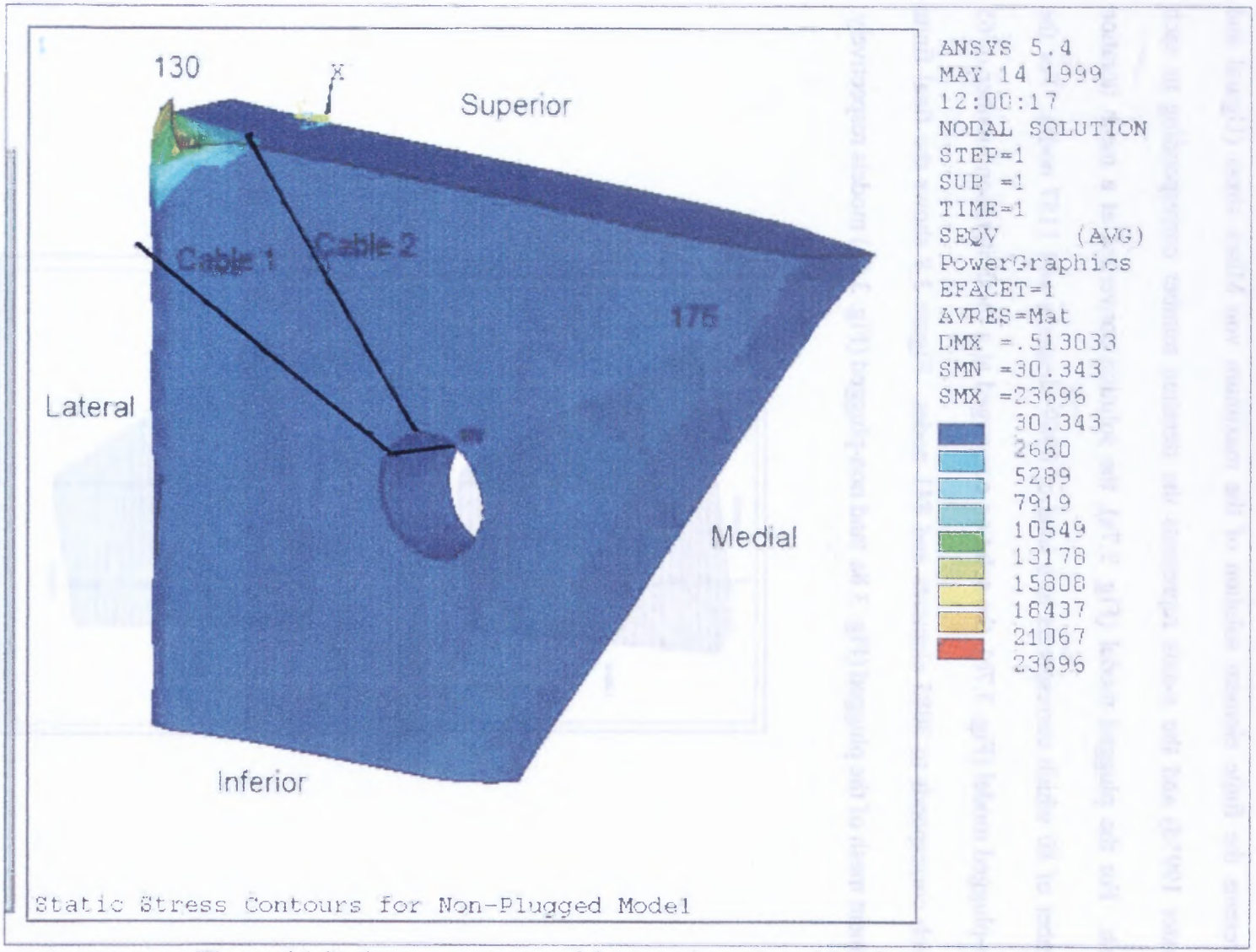

Figure 4.1 Static stress contours of the non-plugged model. *Units are in MPa.*

stress is located at the point where the superior, lateral and posterior surfaces of the implant intersect (node 130 in Fig. 4.1) and has a magnitude of 21.280 GPa (3.086 Mpsi).

A classical calculation was conducted in an effort to validate the FEA results by examining the von Mises stress for the non-plugged model at the point where the maximum stress is located (node 130 in Fig. 4.1). The FEA result of 21.280 GPa (3.086 Mpsi) for the maximum von Mises stress is much higher (Table 4.1) than the calculated result of 10.42×10^{-3} GPa (1.512×10^{-3} Mpsi) from the classical method (Refer to Appendix C for a detailed calculation of von Mises stress). This large difference is attributed to the different methods used by the FEA program and the classical method to determine the geometric properties at the maximum stress location.

Figure 4.2 shows the stress contours of the posterior side of the critical section of the plugged model. The minimum stress is located distally at a point between the inner and outer surfaces of the plug (node 697 in Fig. 4.2), which is close to the hole. The magnitude of the minimum stress is 23.161×10^{-3} GPa (3.358×10^{-3} Mpsi). In most stress analyses, the minimum stress is usually not examined since this stress is least likely to cause failure in the design. However, it is interesting to note that the location of the minimum stress in the plugged model (node 697 in Fig. 4.2) is closer to the hole than that of the non-plugged model (node 176 in Fig. 4.1). Moreover, the magnitude of this stress is lower (Table 4.2) for the plugged model than that for the non-plugged model. This indicates that the presence of the plug in the plugged model caused a change in the distribution pattern of the stress resulting in lower stress near the surface of the hole.

The maximum stress for the plugged model (node 34 in Fig. 4.2) is located at the same location (the point where the superior, lateral and posterior surfaces intersect) as the

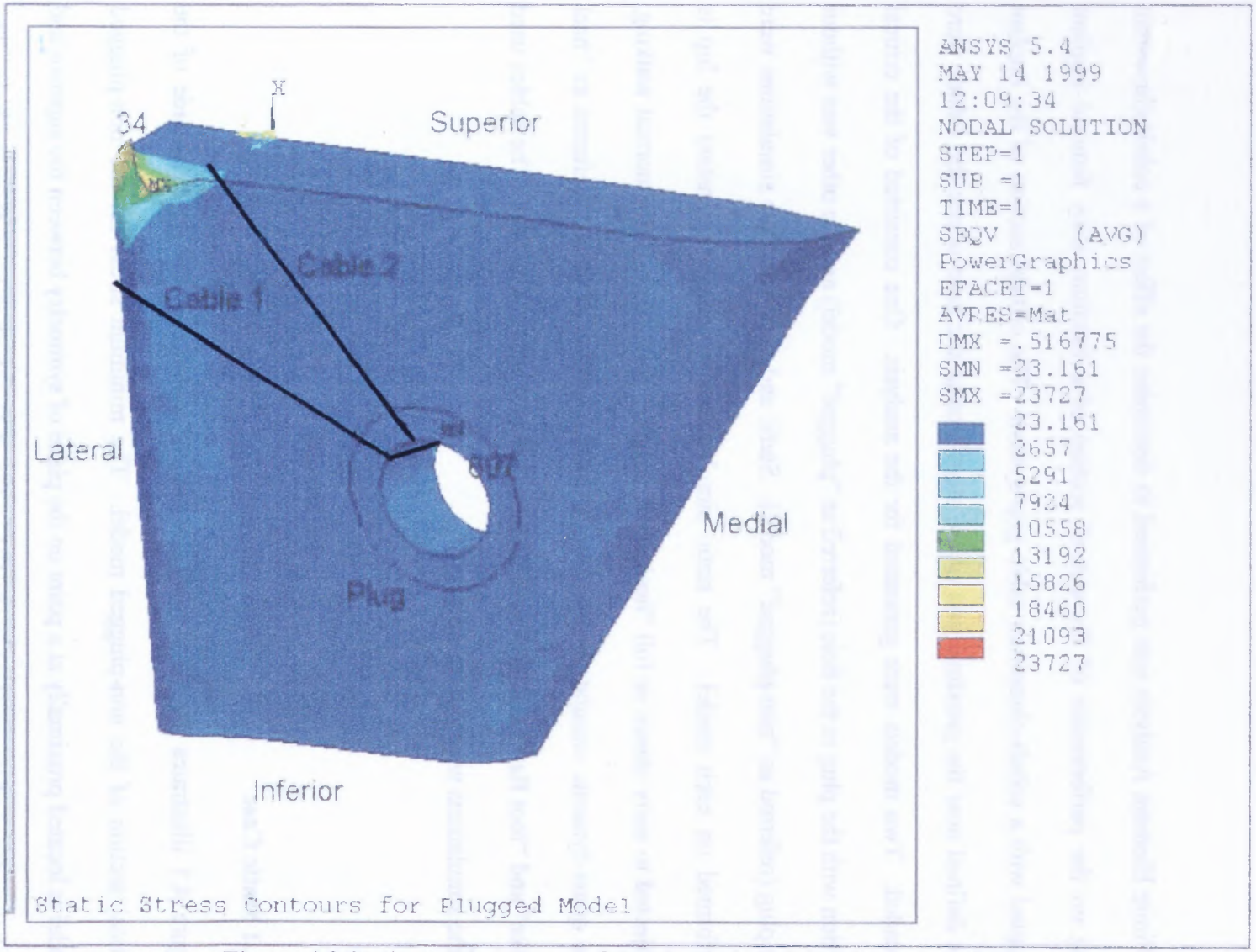

Figure 4.2 Static stress contours of the plugged model. *Units are in MPa.*

non-plugged model (node 130 in Fig. 4.1) and has a magnitude of 21.245 GPa (3.080 Mpsi). This stress is likewise lower (Table 4.2) than that of the non-plugged model, which is 21.280 GPa (3.086 Mpsi), but the difference is small (0.16 %).

Table 4.1 Comparison of FEA and calculated von Mises stress.

Location	FEA Stress (GPa)	Calculated Stress[a] (GPa)	Percent Difference (%)
Maximum[b]	21.280	10.420×10^{-3}	99

[a]Refer to Appendix C for a detailed calculation of von Mises stress.
[b]Located at the point where the superior, lateral and posterior surfaces intersect (node 130 in Fig. 4.1).

Table 4.2 Comparison of von Mises stress between the plugged and non-plugged models.

Plugged				Non-Plugged				Percent Difference (%)	
Minimum Stress		Maximum Stress		Minimum Stress		Maximum Stress		Min.	Max.
Mag. ($x10^{-3}$ GPa)	Loc.[a]	Mag. (GPa)	Loc.[b]	Mag. ($x10^{-3}$ GPa)	Loc.[c]	Mag. (GPa)	Loc.[d]	26.27	0.16
23.161	Node 697	21.245	Node 34	30.343	Node 176	21.280	Node 130		

[a]Located distally at a point near the posterior surface of the model between the inner and outer surfaces of the plug (Fig. 4.2).
[b]Located at the point where the superior, lateral and posterior surfaces of the implant intersect (Fig. 4.2)
[c]Located proximally at a point on the plane of symmetry between the superior and medial surfaces of the implant (Fig. 4.1).
[d]Located at the point where the superior, lateral and posterior surfaces of the implant intersect (Fig. 4.1).

Table 4.3 shows a comparison of the von Mises stress between the plugged and non-plugged models at the cable-implant contact points. The stresses exerted at the contact points by cable 1 for the plugged (Fig. 4.2) and non-plugged (Fig. 4.1) models are 46.599×10^{-2} GPa (67.568×10^{-3} Mpsi) and 49.270×10^{-2} GPa (71.442×10^{-3} Mpsi) respectively. For cable 2, the stresses exerted are 48.054×10^{-2} GPa (69.678×10^{-3} Mpsi) and 75.664×10^{-2} GPa (109.71×10^{-3} Mpsi) for the plugged (Fig. 4.2) and non-plugged

(Fig. 4.1) models respectively. As these results indicate, not only are the geometric stress concentrations, due to the presence of the hole, lower for the plugged model (Table 4.2), but the contact stresses, between the cables and the implant, in the plugged model are lower as well. However, the contact stress exerted by cable 2 exhibits the largest difference between the two models (Table 4.3). This larger difference is attributed to the angle at which the contact force is exerted on the implant by cable 2.

Table 4.3 Comparison of contact stress between the plugged and non-plugged models.

	Plugged	**Non-plugged**	**Percent Difference (%)**
Stress Exerted by Cable 1 (GPa)	46.599×10^{-2}	49.270×10^{-2}	2.47
Stress Exerted by Cable 2 (GPa)	48.054×10^{-2}	74.664×10^{-2}	35.64

4.1.2 Quasi-Dynamic Case

4.1.2.1 Heel Strike Sub-Phase of Stance (0 s < t < 0.15 s): Figures 4.3 (facing page 35) and 4.4 (facing page 36) illustrate the FEA stress contours for the plugged and non-plugged models, respectively, at the full "heel strike" (HS) position of the HS sub-phase of stance (where absolute maximum loading conditions were applied). The minimum stress for the plugged model (node 697 in Fig. 4.3a) is located at the same location (distally at a point between the inner and outer surfaces of the plug) as the plugged model of the static case (node 697 in Fig. 4.2) but has a slightly higher (compare Table 4.2 with Table 4.4) magnitude of 23.411×10^{-3} GPa (3.394×10^{-3} Mpsi). For the non-plugged model (node 176 in Fig. 4.4), the minimum stress is also located at the same location

facing page 35

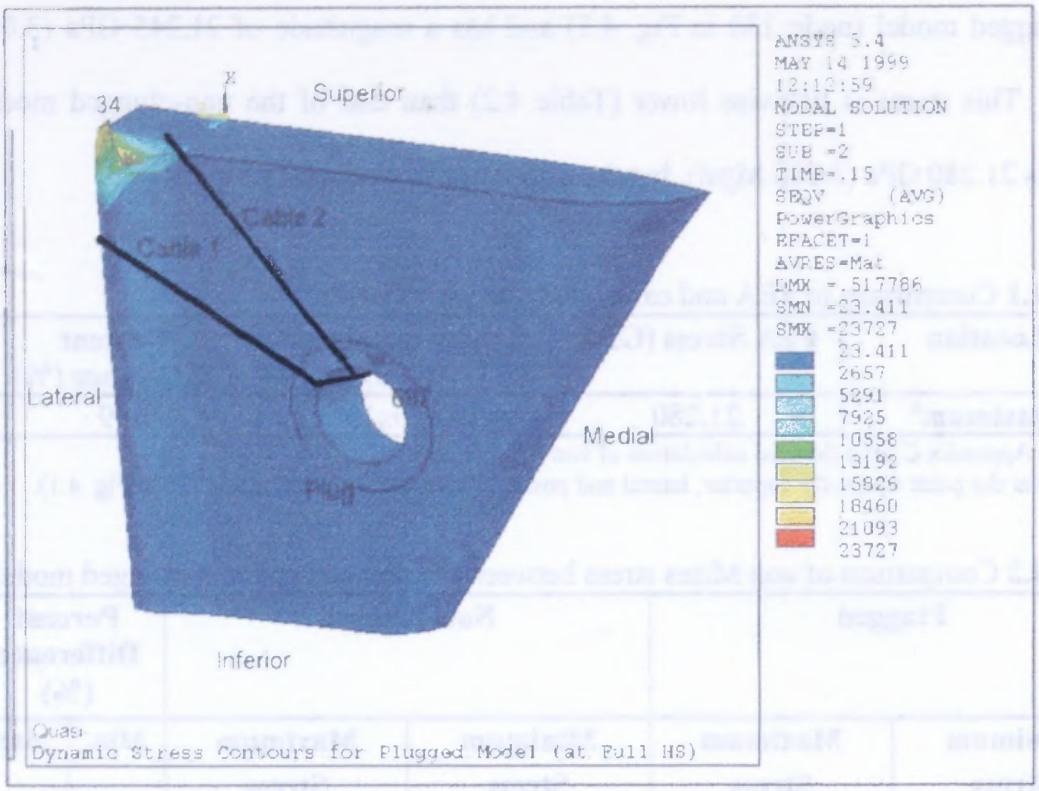

(a)

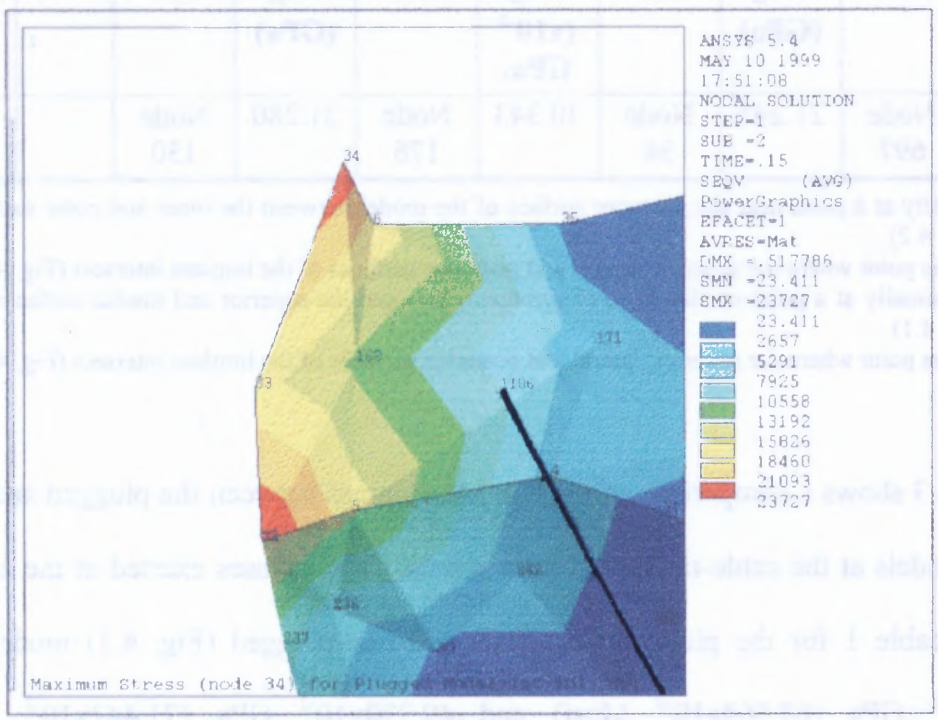

(b)

Figure 4.3 Stress contours of (a) entire plugged model and (b) the maximum location at full "heel strike" (HS) position of HS sub-phase of stance (t = 0.15 s). *Units are in MPa.*

(proximally at a point on the plane of symmetry between the superior and medial surfaces of the implant) as the non-plugged model of the static case (node 176 in Fig. 4.1) but has a slightly lower (compare Table 4.2 with Table 4.4) magnitude of $30.055x10^{-3}$ GPa ($4.358x10^{-3}$ Mpsi). Once again, the minimum stress is lower (Table 4.4) for the plugged model in comparison with the non-plugged.

The maximum stress for the HS quasi-dynamic case of the plugged (node 34 in Fig. 4.3b) and non-plugged (node 130 in Fig. 4.3b) models is located at the same location (the point where the superior, lateral and posterior surfaces intersect) as the models (plugged and non-plugged) for the static case (nodes 34 and 130 in Figs. 4.2 and 4.1 respectively). The magnitudes for the maximum stresses are the same as those for the static case (compare Table 4.2 with Table 4.4) with the stress lower (Table 4.4) for the plugged model (21.245 GPa (3.080 Mpsi)) than that of the non-plugged (21.280 GPa (3.086 Mpsi)).

Table 4.4 Comparison of von Mises stress between the plugged and non-plugged models at full "heel strike" (HS) position of HS sub-phase of stance (t = 0.15 s).

Plugged				**Non-Plugged**				**Percent Difference (%)**	
Min. Stress		**Max. Stress**		**Min. Stress**		**Max. Stress**		**Min.**	**Max.**
Mag. ($x10^{-3}$ GPa)	**Loc.[a]**	**Mag. (GPa)**	**Loc.[b]**	**Mag. ($x10^{-3}$ GPa)**	**Loc.[c]**	**Mag. (GPa)**	**Loc.[d]**	22.11	0.16
23.411	Node 697	21.245	Node 34	30.055	Node 176	21.280	Node 130		

[a]Located distally at a point near the posterior surface of the model between the inner and outer surfaces of the plug (Fig. 4.3).
[b]Located at the point where the superior, lateral and posterior surfaces of the implant intersect (Fig. 4.3b)
[c]Located proximally at a point on the plane of symmetry between the superior and medial surfaces of the implant (Fig. 4.4).
[d]Located at the point where the superior, lateral and posterior surfaces of the implant intersect (Fig. 4.4b).

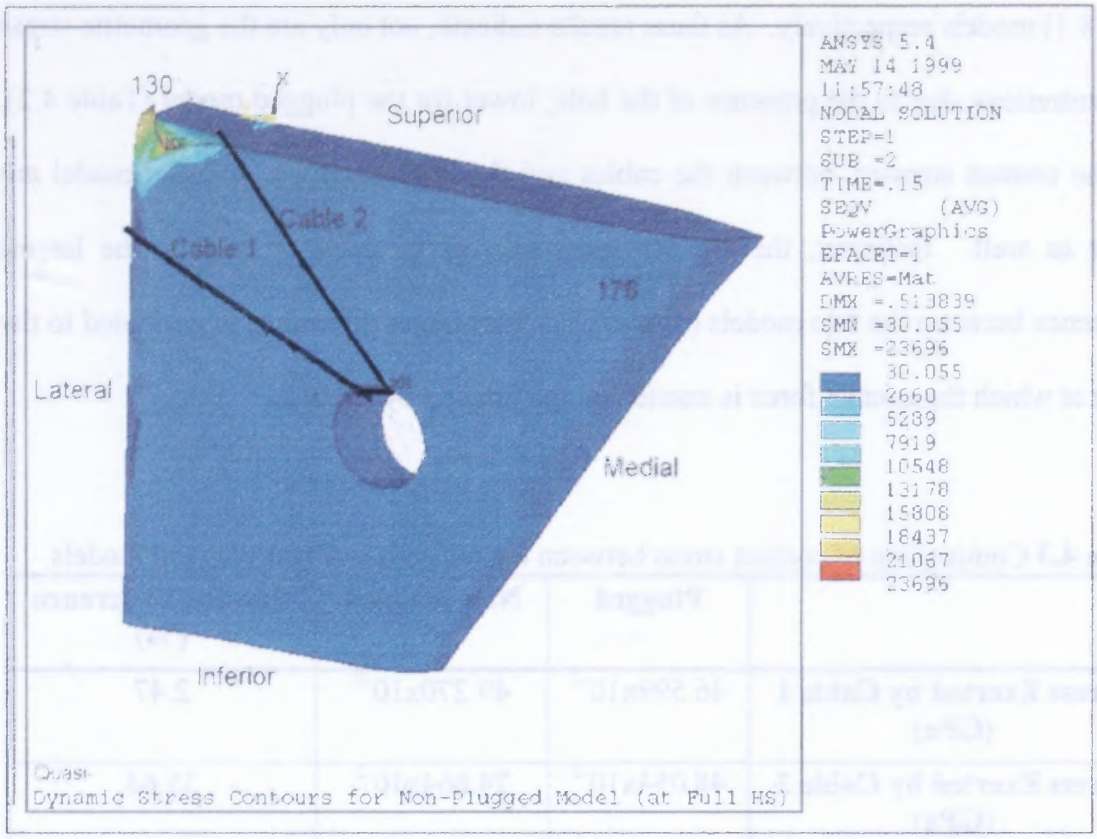

(a)

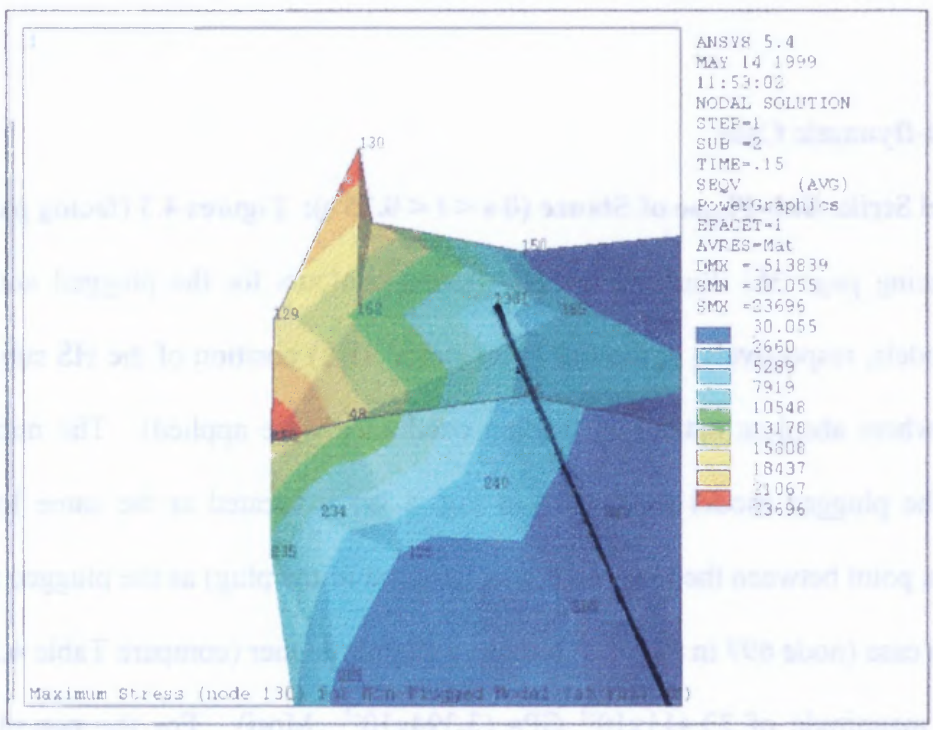

(b)

Figure 4.4 Stress contours of (a) entire non-plugged model and (b) maximum location at full "heel strike" position of HS sub-phase of stance (t = 0.15 s). *Units are in MPa.*

4.1.2.2 Foot Flat Sub-Phase of Stance (0.225 s < t < 0.45 s): Figures 4.5 and 4.6 illustrate the FEA stress contours for the plugged and non-plugged models, respectively, at the full "toe off" (TO) position of the "foot flat" (FF) sub-phase of stance. The minimum stress for the plugged model (node 697 in Fig. 4.5) in this case is located at the same location (distally at a point between the inner and outer surfaces of the plug) as the plugged model of the static (node 697 in Fig. 4.2) and HS sub-phase (node 697 in Fig. 4.3b) cases and has a magnitude of 13.473×10^{-3} GPa (1.954×10^{-3} Mpsi). For the non-plugged model (node 176 in Fig. 4.6), the minimum stress is also located at the same location (proximally at a point on the plane of symmetry between the superior and medial surfaces of the model) as the non-plugged model of the static (node 176 in Fig. 4.1) and HS sub-phase (node 176 in Fig. 4.4b) cases and has a magnitude of (17.986×10^{-3} GPa (2.608×10^{-3} Mpsi)). Once again, the minimum stress is lower (Table 4.5) for the plugged model in comparison with the non-plugged.

The maximum stress for the FF quasi-dynamic case for the plugged (node 34 in Fig. 4.5) and non-plugged (node 130 in Fig. 4.6) models is located at the same location (the point where the superior, lateral and posterior surfaces intersect) as the models (plugged and non-plugged) for the static (nodes 34 and 130 in Figs. 4.2 and 4.1 respectively) and HS sub-phase (nodes 34 and 130 in Figs. 4.3b and 4.4b respectively) cases. The magnitudes for the maximum stresses are 12.745 GPa (1.848 Mpsi) and 12.767 GPa (1.851 Mpsi) for the plugged and non-plugged models respectively. Once again, the stress is lower (Table 4.5) for the plugged model than for the non-plugged, but the difference is small (0.17 %).

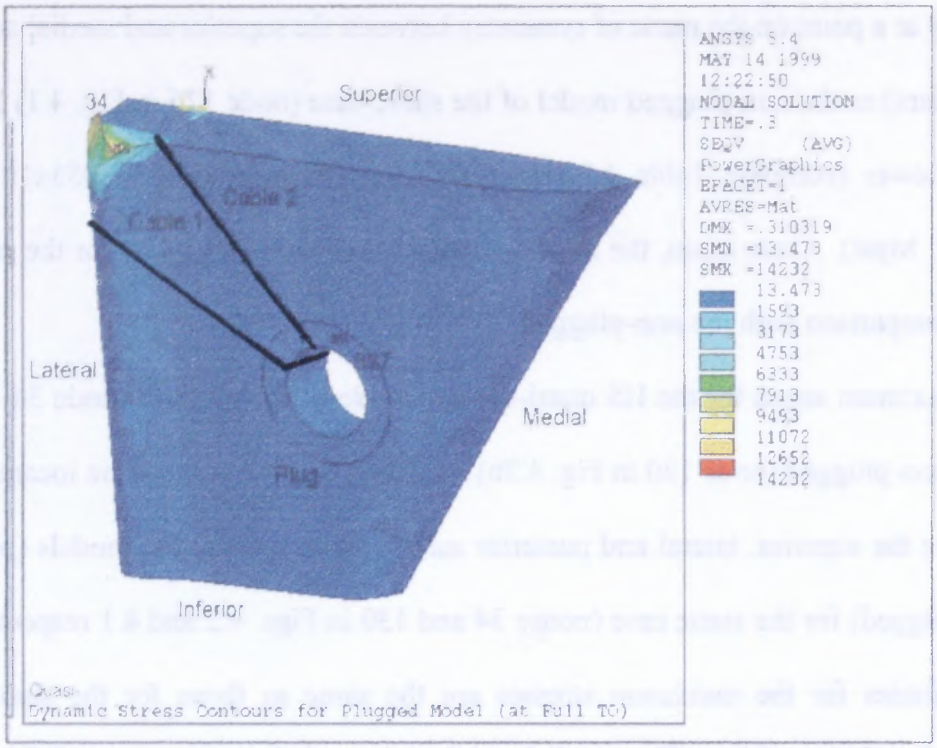

Figure 4.5 Stress contours of plugged model at full "toe off" position of "foot flat" (FF) sub-phase of stance (t = 0.45 s). *Units are in MPa.*

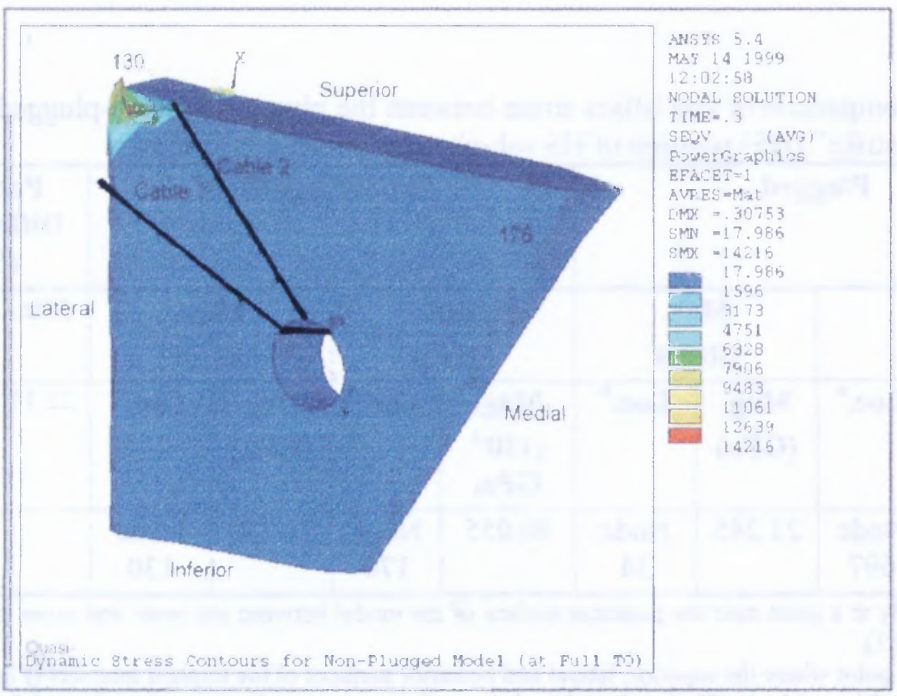

Figure 4.6 Stress contours of non-plugged model at full "toe off" position of "foot flat" (FF) sub-phase of stance (t = 0.45 s). *Units are in MPa.*

Table 4.5 Comparison of von Mises stress between the plugged and non-plugged models at full "toe off" (TO) position of FF sub-phase of stance (t = 0.45 s).

Plugged				**Non-Plugged**				**Percent Difference (%)**	
Minimum Stress		**Maximum Stress**		**Minimum Stress**		**Maximum Stress**		**Min.**	**Max.**
Mag. ($x10^{-3}$ GPa)	**Loc.[a]**	**Mag. (GPa)**	**Loc.[b]**	**Mag. ($x10^{-3}$ GPa)**	**Loc.[c]**	**Mag. (GPa)**	**Loc.[d]**	26.27	0.16
13.473	Node 697	12.745	Node 34	17.986	Node 176	12.767	Node 130		

[a]Located distally at a point near the posterior surface of the model between the inner and outer surfaces of the plug (Fig. 4.5).
[b]Located at the point where the superior, lateral and posterior surfaces of the implant intersect (Fig. 4.5)
[c]Located proximally at a point on the plane of symmetry between the superior and medial surfaces of the implant (Fig. 4.6).
[d]Located at the point where the superior, lateral and posterior surfaces of the implant intersect (Fig. 4.6).

4.1.2.3 The Combined Sub-Phases of Stance: Figure 4.7 illustrates graphs of geometric stress concentration vs. time for the combined sub-phases of stance studied in the quasi-dynamic simulation at the minimum (Fig. 4.7a) and maximum (Fig. 4.7b) locations. The y-axis of the graph shows the von Mises stress produced due to the presence of the hole in the implant. The "heel strike" (HS) region (0 s < t < 0.15 s) of the graph corresponds to the ramped loading conditions applied to the models during each simulation. The "foot flat" (FF) region (0.225 s < t < 0.45 s) corresponds to the stepped loading conditions applied. The geometric stress concentrations, overall, due to the presence of the hole is lower for the plugged model than that for the non-plugged model with the greatest difference exhibited at the minimum (Fig. 4.7a) location.

Figure 4.8 (facing page 39) shows the contact stress vs. time graph, exerted by cable 1 (Fig. 4.8a) and cable 2 (Fig. 4.8b), for the combined sub-phases of stance studied. The contact stresses exerted by cable 1 (Fig. 4.8a), overall, is lower for the plugged model

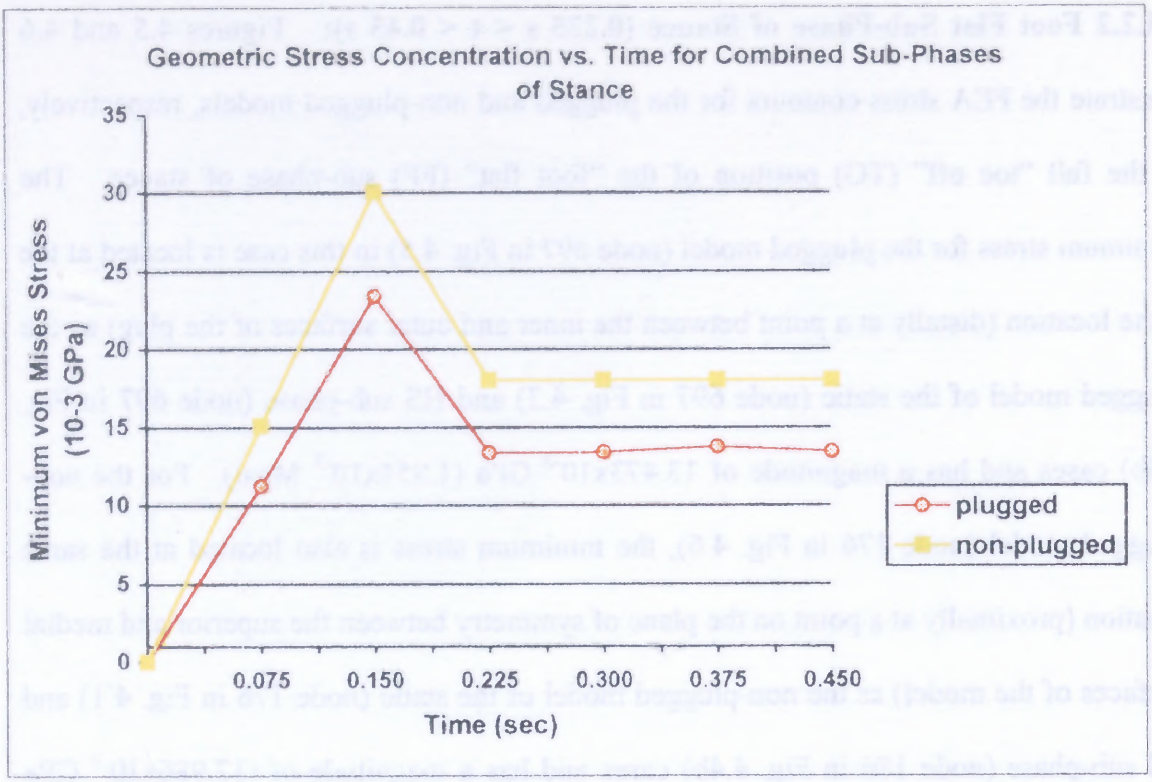

(a)

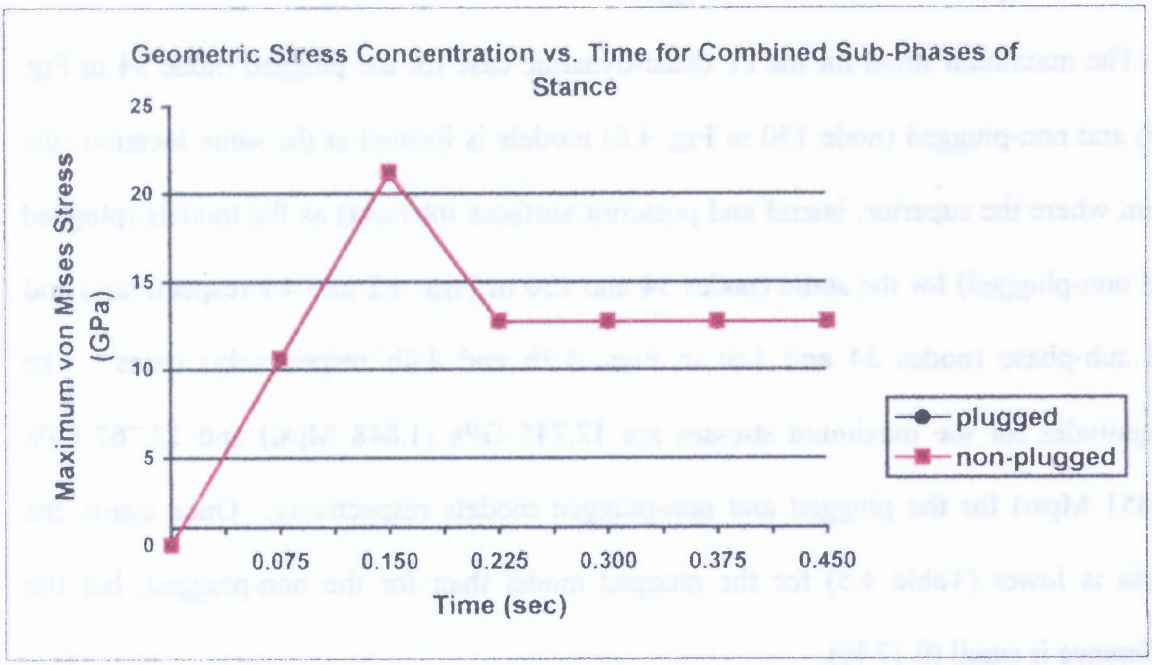

(b)

Figure 4.7 Graph of geometric stress concentration vs. time for the combined sub-phases of stance studied at the (a) minimum and (b) maximum locations.

than that for the non-plugged model but the difference is small (average percent difference is 2.12 % and 0.49 % for the HS and FF sub-phases respectively). The contact stresses exerted by cable 2 (Fig. 4.8b), overall, is also lower for the plugged model than that for the non-plugged model. However, this difference is much larger (average percent difference is 36.31 for both the HS and FF sub-phases) than the difference corresponding to cable 1 (Fig. 4.8a).

4.2 Discussion

Geometric stress concentrations are produced (in both the plugged and non-plugged models of the critical section of the femoral implant) due to the presence of the hole. As the external loading permeates through the implant, the stress around the hole changes. This will involve a change in the diameter and circumference of the hole. The change in circumference gives rise to tangential stresses while the change in diameter gives rise to radial stresses.

Contact stresses result (in both the plugged and non-plugged models) from the force of contact between the cables and the implant on the inside of the hole. During each simulation, a pre-tensioned load was applied along the cables. As a result, contact forces were exerted, parallel to the surface of the implant along the cables, on small areas inside of the hole as the cables were pulled in tension on the posterior and anterior sides of the implant. These applications of force over such small surface areas give rise to high stresses concentrated at the contact areas.

The presence of the plug in the plugged model allowed an interface force to change its line action. As a result, the transmitted force along the line of action may have

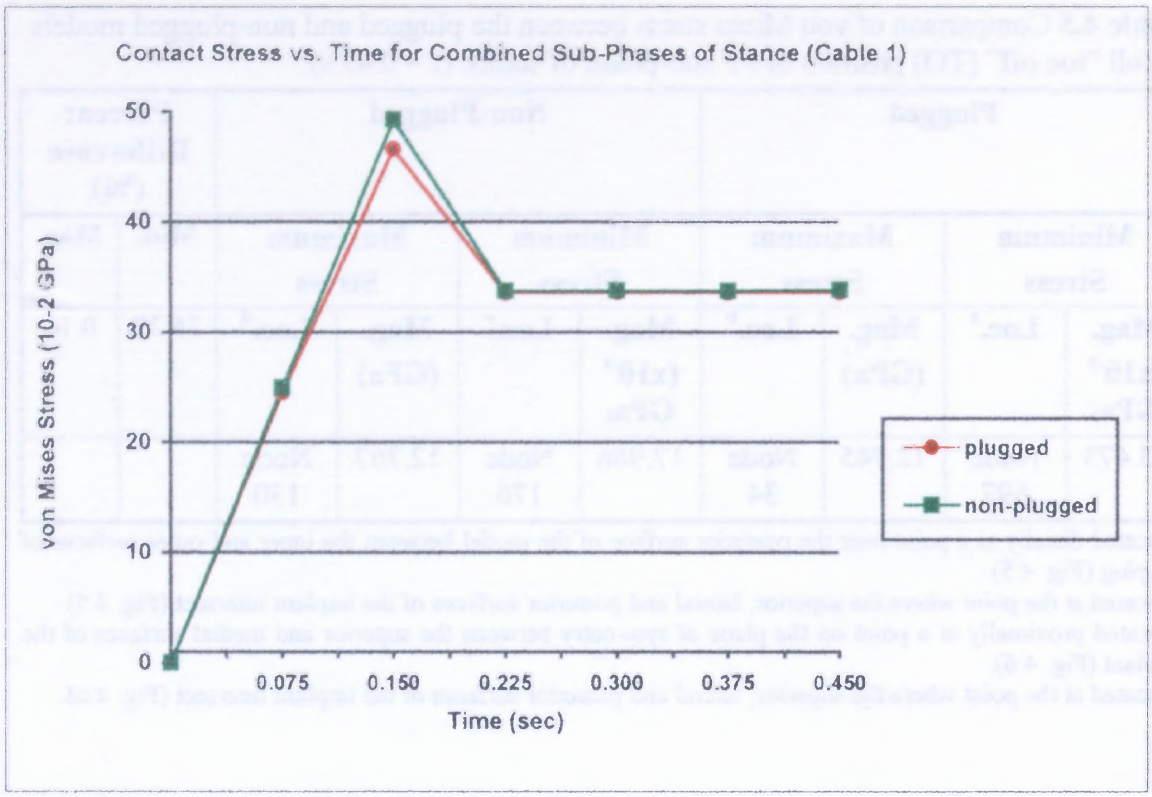

(a)

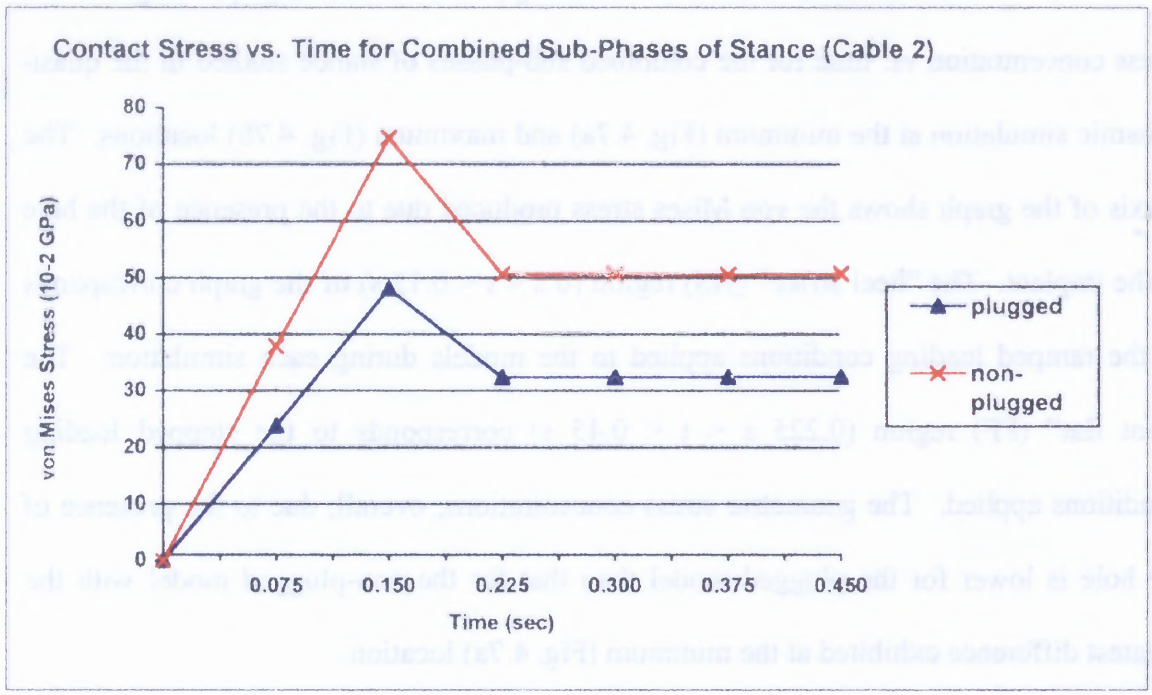

(b)

Figure 4.8 Graph of contact stress vs. time due to (a) cable 1 and (b) cable 2 for the combined sub-phases of stance studied.

decreased in magnitude to a component of the diverted force. This phenomenon shifted the geometric stress concentration away from the surface of the hole providing a resistance to the applied external loading. Thus, a smaller geometry change of the hole is observed and a lower stress is generated (Tables 4.2, 4.4 and 4.5). Moreover, this resistance also resulted in a change in the stress distribution within the implant for the plugged model as evident by the change in the location of the minimum stress between the plugged (Figs. 4.2, 4.3a and 4.5) and non-plugged (Figs. 4.1, 4.4a and 4.6) models.

According to elasticity theory (Ugural and Fenster 1995c), the lower stress in the plugged model can also be attributed to material properties. The use of a cobalt-chromium plug (which is the same material as the cables) in the plugged model provided the hole with even greater resistance to the external loads due to its higher elastic modulus (210 GPa) than that of the titanium alloy implant (116 GPa). As the external loading is resisted by the plug, the surfaces of the implant farthest from the vicinity of the hole undergoes additional deformation due to the resistance, which resulted in a decrease in the stress concentration *difference* (between the plugged and non-plugged models) from the minimum to the maximum location (Tables 4.2, 4.4 and 4.5 and Fig. 4.7).

Since the stress concentration difference (between the plugged and non-plugged models) decreases as the stress is distributed from the minimum to the maximum location (due to the high amount of resistance produced between the titanium alloy (116 GPa) implant and the cobalt-chromium plug (210 GPa)), one may ask, "Why use cobalt-chromium as the material for the plug?" Cobalt-chromium is used as the material for the cables due to its higher tensile strength (1.896 GPa (refer to Table 2.2 in Chapter 2)) than that of titanium alloy (0.965 GPa (refer to Table 2.1 in Chapter 2)). One reason for using

cobalt-chromium as the material for the plug (as opposed to titanium alloy) is that same materials in contact (pre-tensioned cables and the plug) give a better stress distribution in the materials when one material (cable) is loaded and concentrated onto another material (plug). This phenomenon was evident by the lower contact stresses exerted on the plugged model of the implant (Table 4.3 and Fig. 4.8).

Since the presence of cobalt-chromium in the plug and the cables for a plugged implant, overall, results in a better stress distribution, one may also ask, "Why not use cobalt-chromium as the material for the implant?" All orthopaedic metal implants have a considerably higher modulus of elasticity than bone. One reason for using titanium alloy as the material for the implant (as opposed to cobalt chromium alloy) is that titanium alloy is more *mechanically* biocompatible to bone than cobalt-chromium. The modulus for titanium alloy (116 GPa) is only 4 times larger than that of bone (25 GPa (Tarr 1982)) whereas cobalt-chromium (210 GPa) is 8 times larger. Moreover, the composition of most orthopaedic metals contains some elements that are known to cause sensitivity reactions in some individuals (Williams 1977). Sensitivity cases reported (Evans et al. 1974) mostly involved stainless steels and cobalt-chromium alloys, which would indicate that the common elements in these alloys might be the sensitizing constituents. Another reason for using titanium alloy as the implant material is that no evidence has been reported that titanium alloy causes any sensitivity (Williams 1977).

Although the stress concentrations in the plugged model, overall, were lower than that for the non-plugged model in both static and quasi-dynamic cases (Tables 4.2, 4.4 and 4.5 and Fig. 4.7), the difference (between the plugged and non-plugged models) in contact stress (between the cable and the implant stem inside of the hole) exerted by cable 2

(Table 4.3 and Fig. 4.8b) was much greater than the difference in contact stress exerted by cable 1 (Table 4.3 and Fig. 4.8a). This greater difference can be directly attributed to the angle at which each contact force was applied to the implant by each cable. As evident from Figures 4.1-4.6 and Table 3.2 of Chapter 3, the angle of contact force application, θ_{xy}, for cable 1 (25.5°) is smaller than that for cable 2 (64.5°). As a result, the x component of the contact force exerted by cable 2 (201.2 N (45.2 lb)) is higher than that for cable 1 (96.0 N (21.6 lb)). As the x component of the external loading of the implant (F_{xmodel} = 1220 N (274.3 lb)) reaches the area in the implant where the x component of the contact force of cable 2 (201.2 N [45.2 lb]) is also applied, the contact stress produced is much higher for the non-plugged model (Table 4.3 and Fig. 4.8b). This may be due to the combination of the large amount of loading exerted (1220 N and 201.2 N) at this location of the implant and the difference in the elastic properties of the materials (titanium implant (116 GPa) vs. cobalt-chromium cables (210 GPa)).

The quasi-dynamic results for the plugged and non-plugged models at the full HS position (Figs. 4.3 and 4.4 respectively) can be considered approximately equal to the static results (Figs. 4.2 and 4.1 respectively) due to the small differences between the two sets of results (compare Tables 4.2 and 4.4). This indicates that a complete dynamic analysis should be investigated in order to show that the static analysis alone can provide a good approximation prediction.

Since the current study represented the first detailed investigation on performance of femoral implants adjoined with a cable grip systems, experimental studies on this subject are in progress. For this reason, a classical calculation of von Mises stress was conducted in an effort to validate the results of the Finite Element Analysis (FEA). The maximum

von Mises stress for the static case of the non-plugged model was chosen for the classical calculation. According to elasticity (Ugural and Fenster 1995d), von Mises stress in three dimensions is determined by

$$(\sigma_1 - \sigma_2)^2 + (\sigma_2 - \sigma_3)^2 + (\sigma_3 - \sigma_1)^2 = 2\sigma_e^2 \tag{4.1}$$

where σ_e is the von Mises stress and σ_1, σ_2 and σ_3 are the corresponding principal stresses (refer to Appendix B for a detailed calculation of von Mises stress).

The magnitude of the maximum stress obtained from the Finite Element Analysis (FEA) for the static case of the non-plugged model was much higher than the calculated magnitude (Table 4.1). This difference is attributed to the different methods used to determine the geometric properties at the point in the model where the maximum stress was located (node 130 in Fig. 4.1). Since the FEA program determines results at a node (hence a point), geometric properties (i.e. area, moment of inertia, etc.) at a particular node are approximated with very small magnitudes (around 10^{-3}). Since stresses are inversely proportional to geometric properties, the results generated by the program are high due to the small values of the properties. In the classical method (refer to Appendix B), the properties are limited to calculations at the surface rather than at a point. These values are much higher (around 10^{3}) than those approximated in the FEA program (around 10^{-3}), and as a result, the stress obtained by the classical method are lower (Table 4.1) than the FEA by a factor of 10^{3}. This indicates that an experimental test is needed in order to completely validate the FEA results.

CHAPTER 5

CONCLUSIONS AND SUGGESTIONS

5.1 Conclusion

A Finite Element Analysis was performed to determine the effect of a cobalt-chromium plug on the performance of the critical section of a titanium alloy femoral implant coupled with a cobalt-chromium cable grip system The critical section of the implant was defined near the proximal end of the stem around the hole where the cables were threaded. Two models were generated for the analysis. One model consisted of the critical section with the plug in the hole and the other was without the plug. Static and quasi-dynamic simulations were performed on each model. The static simulation represented the instant the hip is subjected to the early stance or full "heel strike" loading conditions during normal walking. The quasi-dynamic simulation represented two sub-phases (referred as 'heel strike" and "foot flat") of stance at a normal walking speed of 4 km/h (3.65 ft/s). The cables used in the simulations were pre-tensioned.

The results of the analysis showed that the geometric stress concentrations as well as the contact stresses in the model with the plug were lower than those in the model without the plug. Based on these results, it can be concluded that the presence of a plug in a femoral implant adjoined with a cable grip system enhances the performance of the implant which can, in turn, prolong its life span.

5.2 Suggestions for Further Study

The results of the current study provide insights into the effect of the plug on the static and quasi-dynamic performance of the modified femoral implant during its initial

use (post-surgery) where no sliding of the cables are expected. However, beyond initial use, sliding of the cables may occur. If this happens frictional affects can become significant. Moreover, cable-sliding results in changes in the angle of the tensile force applied normal to the surface of the implant by the cables. If this happens, the magnitude of the components of the normal forces also change which can lead to an increase or decrease in the contact stress produced by the cables.

Table 4.3 and Figure 4.7 of Chapter 4 showed results of the comparison of contact stress (between the cables and the implant) between the plugged and non-plug models. These results not only showed that the contact stress in the plugged model was lower than that for the non-plug model, but they also showed that the contact stress produced by cable 2 was higher than that for cable 1. This difference in contact stress between the cables is a result of the difference between the angles at which the contact forces were applied parallel to the surface of the implant along the direction of the cables inside of the hole. If these angles are allowed to change constantly due to the sliding of the cables, the performance of the implant may decline with time after initial use if the contact stress produced becomes too high. A further investigation of the sliding mechanism for both models (with and without the plug) is suggested in order to determine the corresponding changes in the stress produced. Such information can provide additional insight into the plug's effect on implant performance beyond its initial use.

APPENDIX A

CALCULATION OF APPLIED LOADS

The purpose of this section is to determine the loads applied on the superior surface and along the cables of the plugged and non-plugged models of the femoral implant adjoined with the cable grip system.

A.1 Superior Surface

The data for the superior surface of each model is determined using the implant load data, which is the joint reaction and abductor muscle forces exerted on the implant at full "heel strike" during normal walking. Figure A.1 shows the schematic of load transformation to the superior surface of the model used in the analysis, which was previously discussed in Chapter 3. The magnitudes of the components of the joint reaction and abductor muscle forces as well as the magnitudes for the moment arm distances are summarized in Table A.1.

Table A.1 Summary of (a) joint reaction and abductor muscle force components and (b) moment arm distances for force and moment calculations. *Information provided by Howmedica Inc.*

(a)

	F_{joint}	F_{muscle}
$F_{resultant}$ (N)	2386.4	1127.3
F_x (N)	2195	-975.1
F_y (N)	755.7	-479.1
F_z (N)	-552.9	301.1

facing page 46

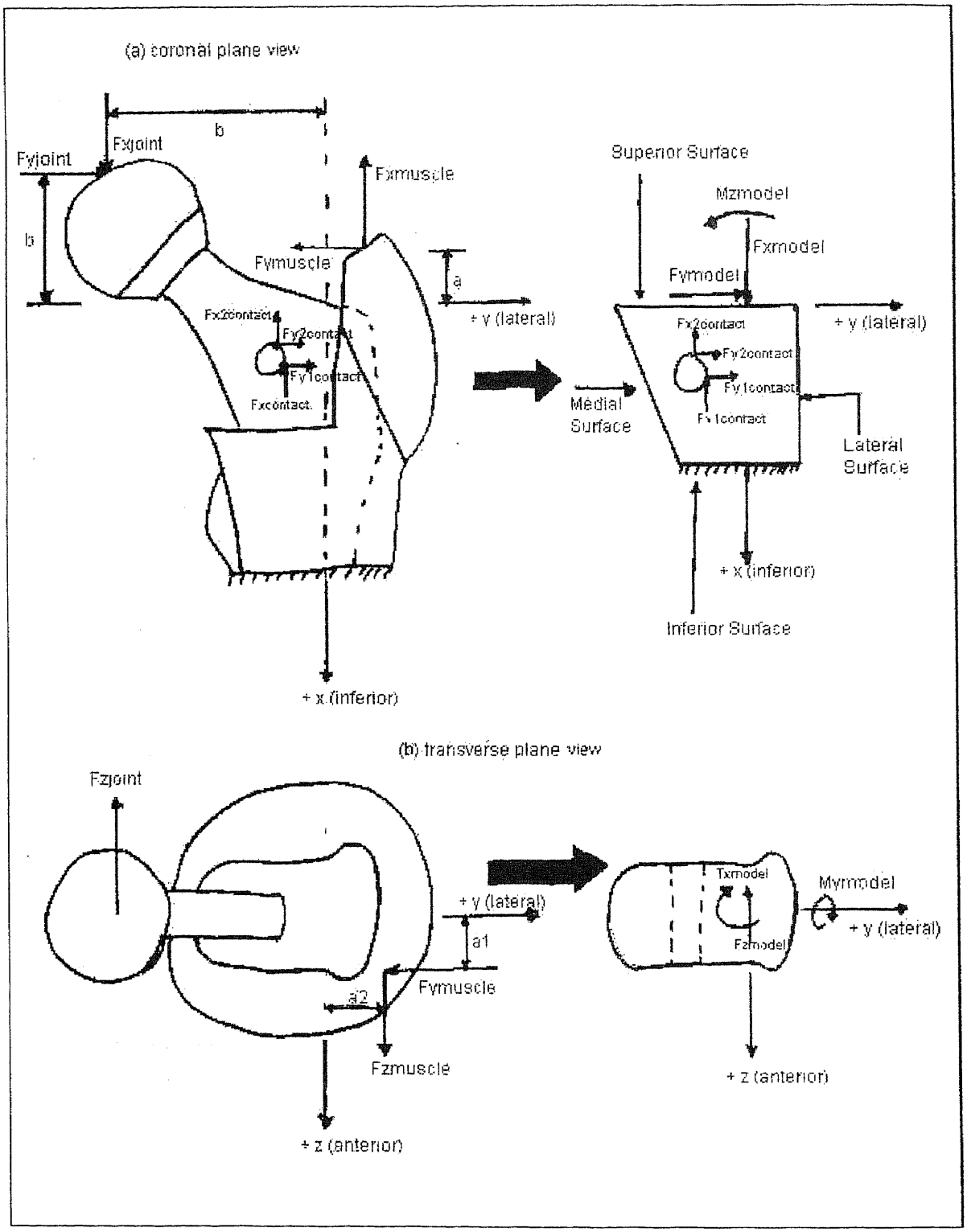

Figure A.1 Schematic of load transformation to the superior surface of the model in the (a) coronal plane and (b) transverse plane views for force and moment calculations.

Table A.1 Summary of (a) joint reaction and abductor muscle force components and (b) moment arm distances for force and moment calculations. *Information provided by Howmedica Inc.* (Continued)

(b)

Moment Arm	Magnitude (mm)
a	4.23
b	27
d	59
a1	1.61
a2	3.07

In the coronal plane (Fig. A.1a), the axial force, F_{xmodel}, produced by the x components of the joint reaction and abductor muscle forces are determined using the equation of force equilibrium (Meriam and Kraige 1992a) on the superior surface in the x (superior-inferior) direction

$$\sum F_x = 0 \qquad (A.1)$$
$$F_{x\,model} = F_{xjoint} - F_{xmuscle}$$
$$F_{x\,model} = 2195N - 975.1N$$
$$F_{x\,model} = 1220N$$

For the shear force, F_{ymodel}, the magnitude is determined using the equation of force equilibrium of the y components of the joint reaction and abductor muscle forces in the y (medial-lateral) direction

$$\sum F_y = 0 \qquad (A.2)$$
$$F_{y\,model} = F_{yjoint} - F_{yxmuscle}$$
$$F_{y\,model} = 755.7N - 479.1N$$
$$F_{y\,model} = 276.6N$$

The bending moment, M_{zmodel}, about the z (posterior-anterior)-axis produced by the x and y components of the joint reaction and abductor muscle forces are determined using the

equation of moment equilibrium (Meriam and Kraige 1992a) on the superior surface about the z-axis

$$\sum M_z = 0 \tag{A.3}$$
$$M_{z\,model} = F_{xjo\,int}d - F_{yjo\,int}b + F_{ymuscle}a + F_{xmuscle}a2$$
$$M_{z\,model} = (2195N)(59mm) - (755.7N)(27mm) + (479.1N)(4.23mm) + (975.1N)(3.07mm)$$
$$M_{z\,model} = 114{,}121.3N - mm(114.1N - m)$$

In the transverse plane (Fig. A.1b), the shear force, F_{zmodel}, produced by the z components of the joint reaction and abductor muscle forces are determined using the equation of force equilibrium on the superior surface in the z direction

$$\sum F_z = 0 \tag{A.4}$$
$$F_{z\,model} = -F_{zjo\,int} + F_{zmuscle}$$
$$F_{z\,model} = -552.9N + 301.1N$$
$$F_{z\,model} = -251.8N$$

The bending moment, M_{ymodel}, about the y-axis produced by the z components of the joint reaction and abductor muscle forces are determined using the equation of moment equilibrium on the superior surface about the y-axis

$$\sum M_y = 0 \tag{A.5}$$
$$M_{y\,model} = -F_{zjo\,int}b + F_{zmuscle}a + F_{xmuscle}a1$$
$$M_{y\,model} = -(552.9N)(27mm) + (301.1N)(4.23mm) + (975.1N)(1.61mm)$$
$$M_{z\,model} = -15{,}324.6N - mm(-15.2N - m)$$

For the torsional moment, T_{xmodel}, the magnitude is determined using the equation of moment equilibrium about the x-axis

$$\sum T_x = 0 \tag{A.6}$$

$$T_{x\,model} = F_{ymuscle}a1 + F_{zmuscle}a2 + F_{zjoint}b$$

$$T_{x\,model} = (479.1N)(1.61mm) + (301.1N)(3.07mm) + (552.9N)(59mm)$$

$$T_{x\,model} = 34{,}317N - mm(34.3.2N - m)$$

A.2 Cables

For the contact force of 223 N (50 lb) applied at the points of contact between the cables and the implant inside of the hole, the components are determined by the angular positions of the cables. Each angle is determined using basic trigonometry. Figure A.2 shows a schematic diagram of the angles for each cable. Based on this configuration, the magnitudes of the angles for each cable can be determined by

$$\theta_{xycable1} = \frac{90 - \beta}{2}$$

$$\theta_{xycable1} = 45 - \frac{\beta}{2} \tag{A.7}$$

$$\theta_{xycable2} = \theta_{cable1} + \beta$$

where β is the angle of separation between cables 1 and 2. The magnitude for β is 39°, which represents the case where the cables are close to each other inside of the hole but do not overlap (information provided by Howmedica Inc.). Substituting the magnitude for β into Equation A.1 yields 25.5° and 64.5° for $\theta_{xycable1}$ and $\theta_{xycable2}$ respectively. Substituting these angles into the trigonometric expressions

$$\begin{aligned} F_{xcable1} &= 223\sin\theta_{xycable1} \\ F_{ycable1} &= 223\cos\theta_{xycable1} \\ F_{xcable2} &= 223\sin\theta_{xycable2} \\ F_{ycable2} &= 223\cos\theta_{xycable2} \end{aligned} \tag{A.8}$$

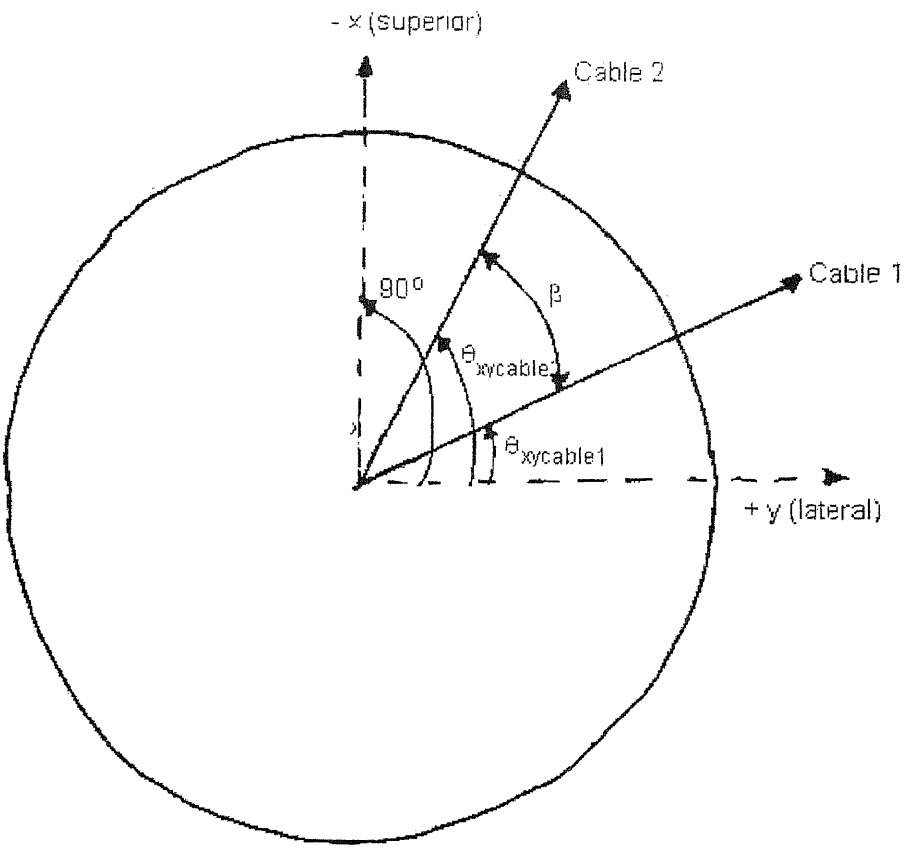

Figure A.2 Schematic diagram of angular positions of cables inside of the hole.

yields the x and y components (Figure A.1 and Table A.2) of the contact forces exerted at the points between the cables and the implant inside of the hole. Since it is assumed that the cables are not pulled in a direction perpendicular to the coronal plane of the implant away from the vicinity of the hole, the contact force angle, θ_{xz}, as well as the z component of the contact force, F_{zcable}, are equal to zero.

Table A.2 Summary of contact forces exerted on the implant inside of the hole by the cables.

	Cable 1	**Cable 2**
Contact Force Angle θ_{xy} (°)	25.5	64.5
$F_{resultant}$ (N)	223	223
F_{xcable} (N)	-96.0	-201.2
F_{ycable} (N)	201.2	96.0
F_{zcable} (N)	0	0

APPENDIX B

DESCRIPTION OF LOADING AT FULL "HEEL STIKE" DURING NORMAL WALKING

The purpose of this section is to provide a description of the components of the joint reaction and abductor muscle forces exerted on the femur at full "heel strike" during normal walking. Howmedica Incorporated provided the actual data presented in the following sections.

B.1 Joint Reaction Force

During normal walking, the maximum joint reaction force occurs in early stance (full "heel strike") at around 7% percent of the gait cycle. At this point (Fig. B.1), the resultant joint reaction force exerted on the head of the femur is approximately 3.4 times body weight (BW). This force consists of the following components (defined with respect to the external coordinate system (CS) defined by the body at rest):

$$\left.\begin{aligned} F_x &= 3.25 \text{ BW (inferior)} \\ F_y &= 0.63 \text{ BW (lateral)} \\ F_z &= 0.77 \text{ BW (anterior)} \end{aligned}\right\} F = 3.4 \text{ BW} \qquad \text{(B.1)}$$

Within the body CS, the femur is oriented in 9° of adduction and 27° of flexion (Fig. B.1). After transformation from the body CS to the femur CS, the joint reaction force is represented as

facing page 51

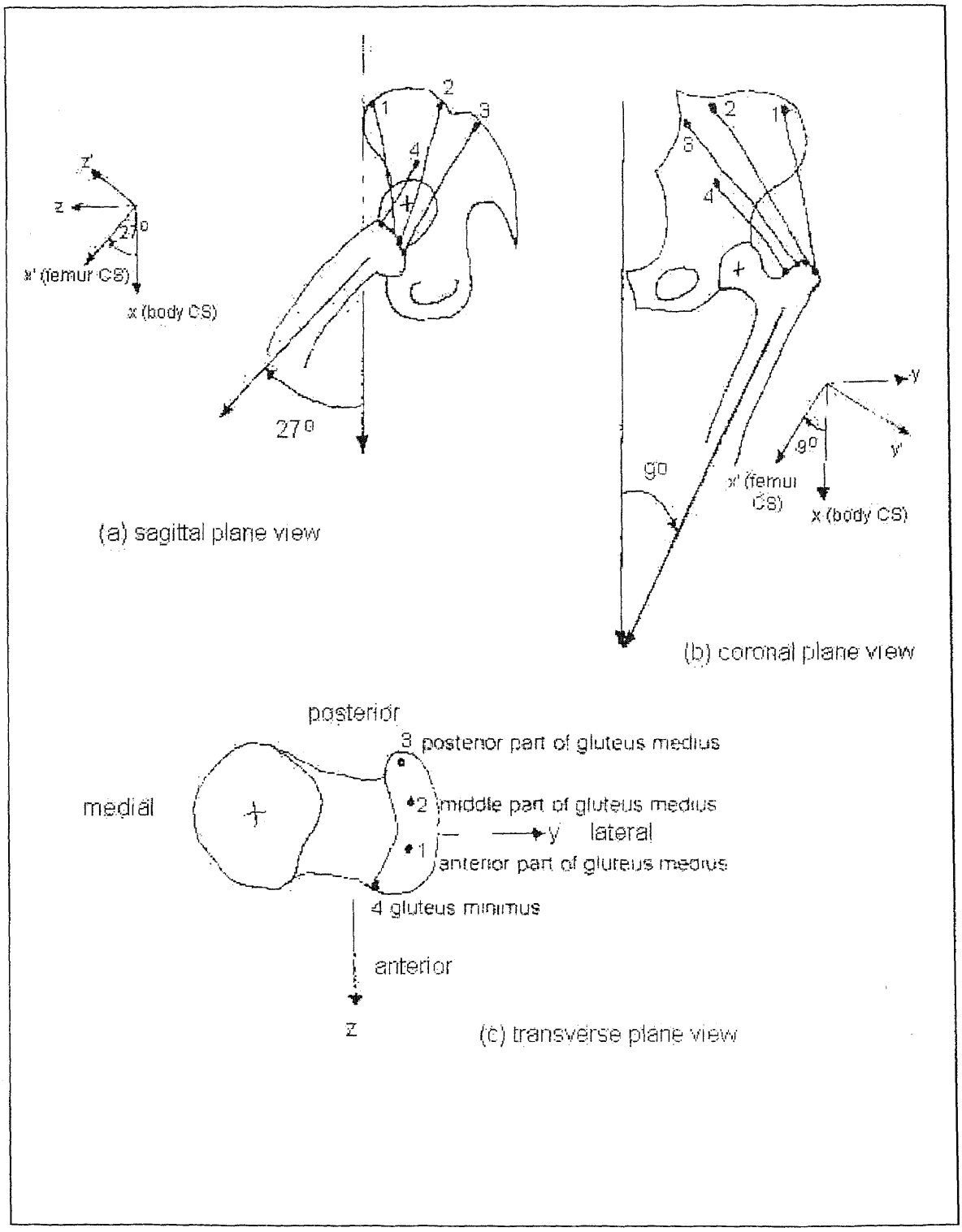

Figure B.1 Orientation of left femur within the body at full "heel strike" position of stance in the (a) sagittal plane (b) coronal plane and (c) transverse plane views.

$$\left.\begin{aligned} F_x &= 3.13 \text{ BW (inferior)} \\ F_y &= 1.08 \text{ BW (lateral)} \\ F_z &= -0.79 \text{ BW (anterior)} \end{aligned}\right\} F = 3.4 \text{ BW} \qquad \text{(B.2)}$$

in the femur CS. For an average body weight of 700.2 N (157.4 lb) the joint reaction force becomes

$$\left.\begin{aligned} F_x &= 2195 \text{ N (492.7 lb) (inferior)} \\ F_y &= 755.7 \text{ N (169.9 lb) (lateral)} \\ F_z &= -552.9 \text{ N (-124.3 lb) (anterior)} \end{aligned}\right\} F = 2386.4 \text{ N (535.8 lb)} \qquad \text{(B.3)}$$

B.2 Muscle Force

The joint reaction force exerted on the femur is resisted by the ground reaction force transmitted to the distal femur as well as the force of contraction of the muscle force generated on the greater trochanter, principally, by the gluteus medius and minimus (Fig. B.1). Table B.1 provides a summary of the magnitudes of the forces exerted by the gluteus medius and minimus in the femur coordinate system (CS). In the analysis, this group of muscle forces is represented as a single muscle force (Table B.1) by the summation of the individual force magnitudes.

Table B.1 Magnitudes of forces exerted by the gluteus medius and minimus on the greater trochanter of the femur.

	Anterior Part of Gluteus Medius	**Middle Part of Gluteus Medius**	**Posterior Part of Gluteus Medius**	**Gluteus Minimus**	**Total**
F_x (N)	-248.2	-135.7	-251.8	-339.4	-975.1
F_y (N)	-62.3	-46.3	-182.8	-187.7	-479.1
F_z (N)	178.4	61.3	16.9	44.5	301.1
Resultant (N)	311.9	155.9	311.6	390.4	1127.4

APPENDIX C

CALCULATION OF VON MISES STRESS

The purpose of this section is to calculate the von Mises stress, using the classical method, for the maximum stress exerted on the superior surface of the non-plugged model for the static case. The calculation is conducted in an attempt to validate the solution obtained from the Finite Element Analysis.

C.1 Calculation of State of Stress

Figure C.1a provides a schematic of the superior surface of the model. Due to symmetry in geometry and loading about the coronal plane, only half (posterior side) of the surface is used for the study. We begin the calculation with the determination of the state of stress at point A (Fig. C.1b). This point is chosen for the von Mises stress calculation since it is the location where the maximum stress is exerted on the non-plugged model (Refer to Fig. 4.1 in Chapter 4).

The state of stress at point A (Fig. C.1b) results from the forces and moments applied to the superior surface (Fig. C.1a). The magnitudes of these forces and moments (Table C.1) were calculated in Appendix A.

Table C.1 Magnitudes of forces and moments applied to the superior surface.

	Resultant	**x component**	**y component**	**z component**
Force (N)	1276.1	1220	276.6	-251.8
Moment (N-m)	120.1	34.3	-15.2	114.1

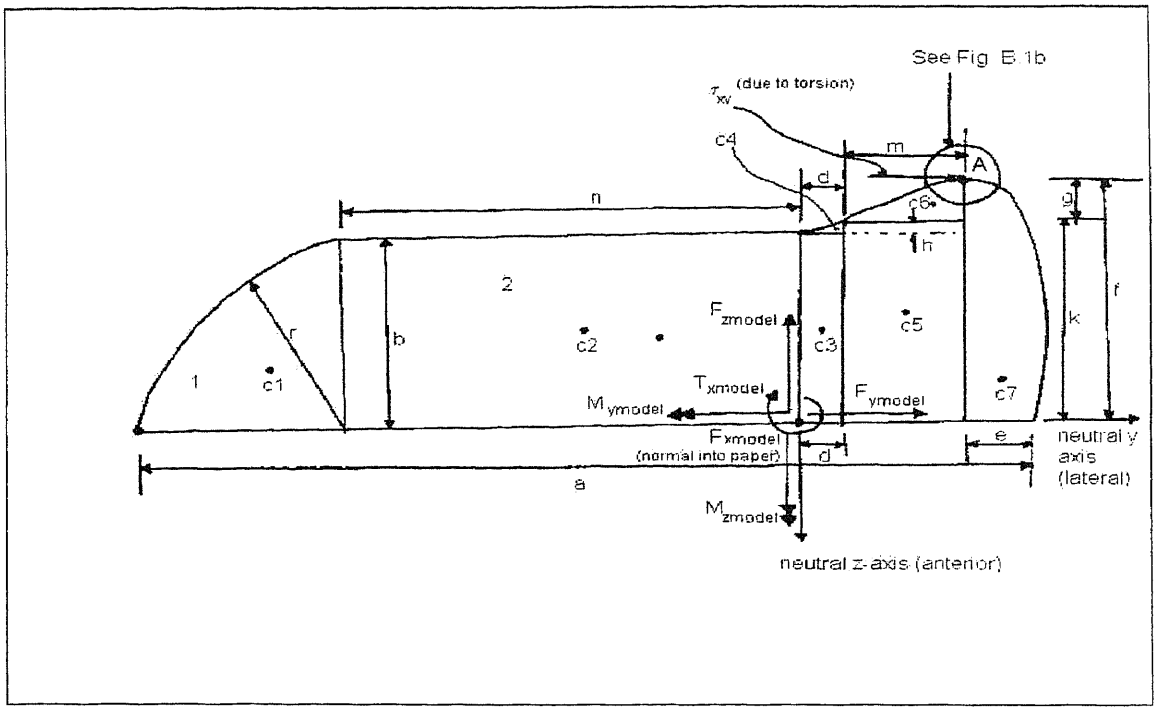

(a)

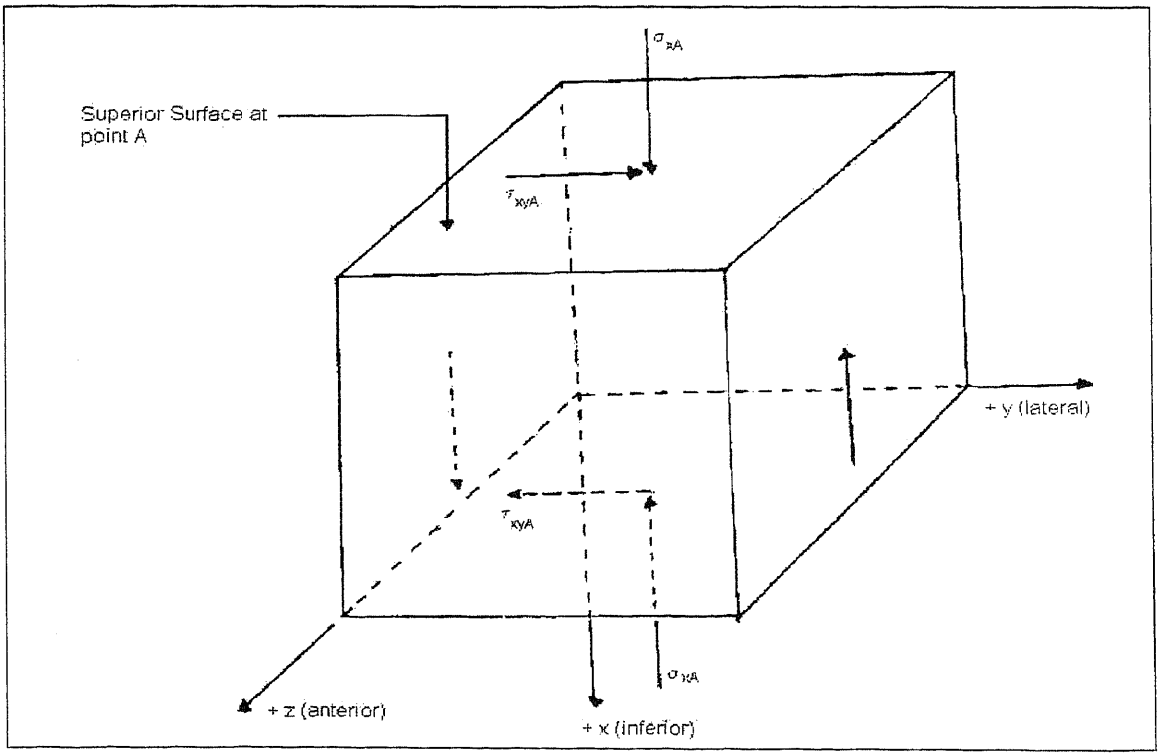

(b)

Figure C.1 Schematic of (a) superior surface and (b) state of stress at point A for von Mises stress calculation.

A normal stress, σ_{xA}, is exerted on point A (Fig. C.1b) and is produced by the axial force, F_{xmodel}, and the bending moments, M_{zmodel} and M_{ymodel} (Fig. C.2a). Since the forces, F_{ymodel} and F_{zmodel}, only produce shear loading on the superior surface, and the bending moments, M_{zmodel} and M_{ymodel}, only produce normal loading on the surface (in the x direction), the normal stresses, σ_{yA} and σ_{zA}, are equal to zero. The magnitude of the normal stress, σ_{xA}, is obtained through the summation of the axial and bending stresses (Ugural and Fenster 1995f)

$$\sigma_{xA} = \sigma_{xAaxial} + \sigma_{xAbending}$$

$$\sigma_{xA} = \frac{F_{x\,mod\,el}}{A_C} + \frac{M_{y\,mod\,el}\,z}{I_y} - \frac{M_{z\,mod\,el}\,y}{I_z} \qquad \text{(C.1)}$$

where

- y = perpendicular distance from the neutral z-axis to point A
- z = perpendicular distance from the neutral y-axis to point A
- A_C = cross-sectional area of the superior surface
- I_y = moment of inertia about the neutral y-axis
- I_z = moment of inertia about the neutral z-axis

A shear stress, τ_{xyA}, is exerted on point A (Fig. C.1b) and is produced by the shear force, F_{ymodel}, and the torsional moment, T_{xmodel} (Fig. C.1a). Since the torsional shear (Fig. C.1a) is in the y direction at point A (which results from the clockwise rotation of T_{xmodel}), and the transverse shear due to the shear force F_{zmodel} (Fig. C.1a) is zero at the outer most edge of the surface (Hibbeler 1994b), the shear stress, τ_{xzA}, is equal to zero. Since the external loading is only exerted on the superior surface of point A (Fig. C.1b), the shear stress, τ_{yzA}, is also equal to zero. The magnitude of the shear stress, τ_{xyA}, is

obtained through the summation of the transverse and torsional stresses (Ugural and Fenster 1995f)

$$\tau_{xyA} = \tau_{xyAtransverse} + \tau_{xyAtorsion}$$
$$\tau_{xyA} = \frac{F_{y\,mod\,el}Q}{I_y t} + \frac{T_{x\,mod\,el}z}{J_x} \qquad \text{(C.2)}$$

where

- t = the width of the cross-sectional area measured at point A where τ_{xzA} is calculated
- J_x = polar moment of inertia about the neutral x-axis
- Q = first moment about neutral z-axis of the area beyond point A at which τ_{xzA} is calculated

C.1.1 Geometric Properties

In order to determine the state of stress at point A (Fig. C.1b) using Equations (C.1) and (C.2), the geometric properties must be calculated. Table C.2 provides a summary of the values for the dimensions of the shapes on the superior surface (Fig. C.1a).

Table C.2 Dimensions for geometry of shapes on superior surface (Fig. C.1a).

Dimension	Magnitude (mm)
a	50
b	10
d	3.4
e	1.2
f	11.5
g	0.9
h	0.6
k	10.6
m	3.4
n	32
r	10

Due to the complexity of the area of the superior surface, it is necessary to calculate the geometric properties of the entire area as a sum of simpler areas with calculable geometric shapes (Meriam and Kraige 1992b). As illustrated in Figure C.1a, the superior surface is divided into seven simple shapes. Shape 1 is a quarter circular arc. Shapes 2, 3 and 5 are rectangles. Shape 4 is a sub-parabolic area. Shape 6 is a parabolic area, and shape 7 is an elliptical quadrant. The centroidal coordinates y_c and z_c (Meriam and Kraige 1992c) of each shape is summarized in Table C.3.

Table C.3 Calculation of centroidal coordinates for each shape (Fig. C.1a) on the superior surface.

Shape	y_c (mm)	z_c (mm)
1	4.24	4.24
2	16	5
3	1.7	5
4	2.55	0.18
5	1.7	5.3
6	1.28	0.54
7	0.51	4.88

Using the parallel axis theorem (Meriam and Kraige 1992b) the moments of inertia, I_y and I_z, and the polar moment of inertia, J_x, for the superior surface is calculated by

$$\begin{aligned} I_y &= \sum \bar{I}_y + \sum A d_z^2 \\ I_z &= \sum \bar{I}_z + \sum A d_y^2 \\ J_x &= I_y + I_z \end{aligned} \qquad \text{(C.3)}$$

where I_y and I_z are the moments of inertia for each simple area about the centroidal y and z axes respectively d_y is the perpendicular distance between the centroidal z-axis of each simple shape and the neutral z axis of the superior surface and d_z is the perpendicular distance between the centroidal y-axis of each simple shape and the neutral y-axis of the superior surface.

Table C.4 summarizes the calculations of ΣI_y, ΣI_z, $\Sigma A d_y^2$ and $\Sigma A d_z^2$. The values are 3.94×10^3 mm^4, 27.93×10^3 mm^4, 186.75×10^3 mm^4, and 11.85×10^3 mm^4 respectively. Substituting these values into Equation (C.3) yields 15.79×10^3 mm^4, 214.68×10^3 mm^4 and 230.47×10^3 mm^4 for I_y, I_z and J_x respectively. The sum total of the areas of the shapes, (482.14 in Table C.4), is also equal to the cross-sectional area, A_c, of the entire superior surface.

Table C.4 Calculation of inertial data for each shape on superior surface.

Shape	**A (mm^2)**	**d_y (mm)**	**d_z (mm)**	**Ad_y^2 (mm^4)**	**Ad_z^2 (mm^4)**	**I_y (mm^4)**	**I_z (mm^4)**
1	78.54	36.24	4.24	103149.54	1411.96	548.78	548.78
2	320.00	16.00	5.00	81920.00	8000.00	2666.67	27306.67
3	34.00	1.70	5.00	98.26	850.00	283.33	32.75
4	0.68	2.55	10.18	4.42	70.47	0.035	4.72
5	36.04	5.10	5.30	937.40	1012.36	337.45	34.72
6	2.04	5.52	10.96	62.16	245.05	0.71	4.72
7	10.84	7.31	4.88	579.25	258.15	100.16	1.09
Totals	**482.14**			**186751.03**	**11847.99**	**3937.14**	**27933.45**

The first moment about the neutral z-axis, Q, is obtained by (Ugural and Fenster 1995f)

$$Q = \bar{y}A' \tag{C.4}$$

where A' is the area beyond point A at which τ_{xyA} is calculated and y is the distance to the centroid of A' measured from the neutral z-axis. The area of interest, where τ_{xyA} is calculated, is illustrated by the shaded region in Figure C.2. The width of this area, t, is 11.5 mm. The area of shape 7 (the elliptical quadrant) is the only area included in the shaded region. Therefore, y is equal to the perpendicular distance, dy, from the neutral z-axis and A' is equal to the area of shape 7. The values for y and A' are taken directly from Table C.4 and are 7.31 mm and 10.84 mm^2 respectively. Substituting these values into equation C.4 yields 79.24 mm^3 for Q.

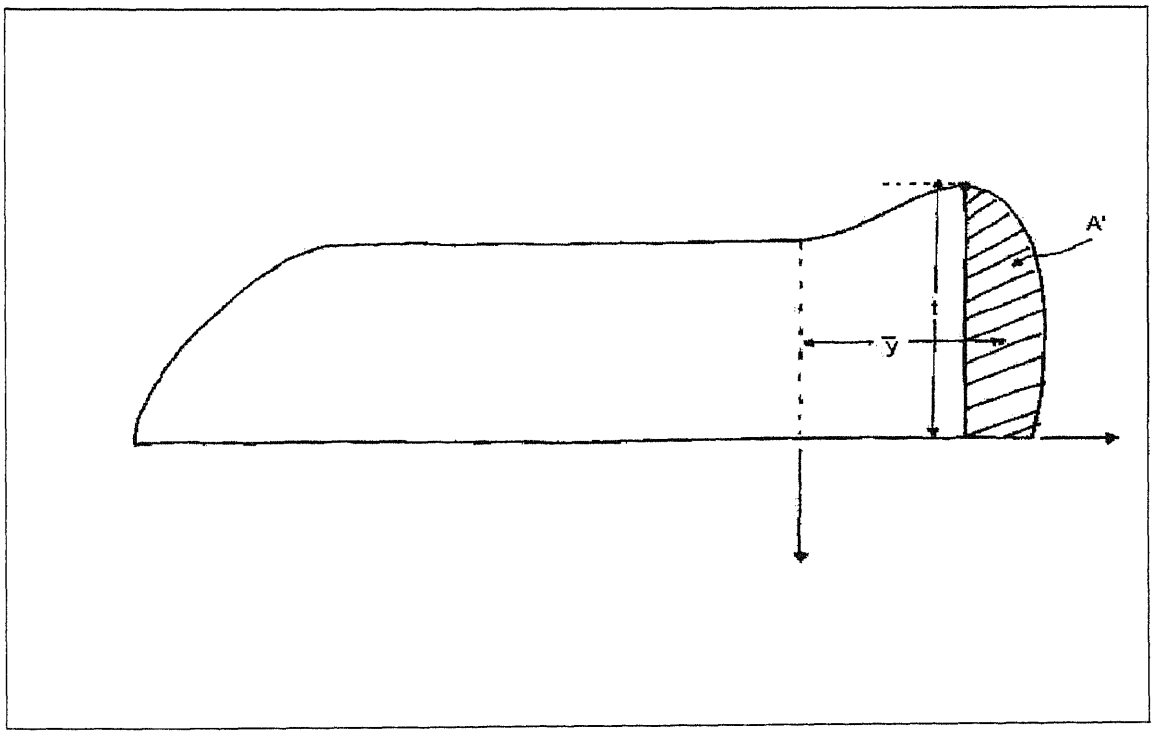

Figure C.2 Schematic of area beyond point A at which τ_{xyA} is calculated.

Table C.5 provides a summary of all of the geometric properties previously calculated. Substitution of these values into Equations C.1 and C.2 yields 9.97 MPa and 1.83 MPa for the stresses σ_{xA} and τ_{xzA} respectively.

Table C.5 Summary of calculated geometric properties.

Geometric Property	Value
A_c (mm^2)	482.14
I_y (mm^4)	15.79×10^3
I_z (mm^4)	214.68×10^3
Q (mm^3)	79.24
t (mm)	11.5
y (mm)	6.8
z (mm)	11.5
J_x (mm^4)	230.47×10^3

C.2 Calculation of Principal Stresses

The next step in the determination of von Mises stress at point A is the calculation of the principal stresses. In three dimensional form, the principal stresses are determined by the stress cubic equation (Ugural and Fenster 1995e)

$$\sigma_p^3 - I_1\sigma_p^2 + I_2\sigma_p - I_3 = 0 \tag{C.5}$$

where I_1, I_2 and I_3 are the stress invariants (Ugural and Fenster 1995e) determined by

$$
\begin{aligned}
I_1 &= \sigma_x + \sigma_y + \sigma_z \\
I_2 &= \sigma_x\sigma_y + \sigma_x\sigma_z + \sigma_y\sigma_z - \tau_{xy}^2 - \tau_{yz}^2 - \tau_{xz}^2 \\
I_3 &= \begin{vmatrix} \sigma_x & \tau_{xy} & \tau_{xz} \\ \tau_{xy} & \sigma_y & \tau_{yz} \\ \tau_{xz} & \tau_{yz} & \sigma_z \end{vmatrix}
\end{aligned}
\tag{C.5a}
$$

and the three roots of Equation C.4 are the principal stresses.

There are many methods in common use for solving a cubic equation. A practical approach for determining the roots of the stress cubic equation (Eqn. (C.5)) involves solving the expressions (Ugural and Fenster 1995e)

$$
\begin{aligned}
\sigma_a &= 2S[\cos(\alpha/3)] + \frac{1}{3}I_1 \\
\sigma_b &= 2S\{[\cos(\alpha/3) + 120^\circ]\} + \frac{1}{3}I_1 \\
\sigma_c &= 2S\{[\cos(\alpha/3) + 240^\circ]\} + \frac{1}{3}I_1
\end{aligned}
\tag{C.6}
$$

where the constants of Equation C.6 are given by

$$S = \left(\frac{1}{3}R\right)^{1/2}$$

$$\alpha = \cos^{-1}\left(-\frac{Q}{T}\right)$$

$$R = \frac{1}{3}I_1^2 - I_2 \qquad \text{(C.6a)}$$

$$Q = \frac{1}{3}I_1 I_2 - I_3 - \frac{2}{27}I_1^3$$

$$T = \left(\frac{1}{3}R^3\right)^{1/2}$$

The principal stresses found from Equation (C.6) using this approach are reassigned using numerical subscripts so that $\sigma_1 > \sigma_2 > \sigma_3$.

The state of stress for point A was determined as 9.97 MPa and 1.83 MPa for the stresses σ_{xA} and τ_{xzA} in section C.1. Substituting these magnitudes into Equation (C.5a) yields 9.97 MPa, -3.35 MPa, and 0 MPa for the stress invariants I_1, I_2 and I_3 respectively. Substituting these magnitudes into Equation (C.6a) yields the values for the constants of the stress cubic equation (Eqn. (C.6)), which are listed in Table C.6.

Table C.6 Constants of stress cubic equation (Eqn. (C.6)) obtained from Equation (C.6a).

Constant	Value
S	3.47
α	4.97
R	36.48
Q	-84.47
T	42.39

After substitution of S, α, and I_1 into Equation. (C.6) and reassigning σ_a, σ_b, and σ_c with numerical subscripts, the principal stresses are determined as

of delamination progression, and leads to better assessment and timing for implementation of rehabilitation measures.

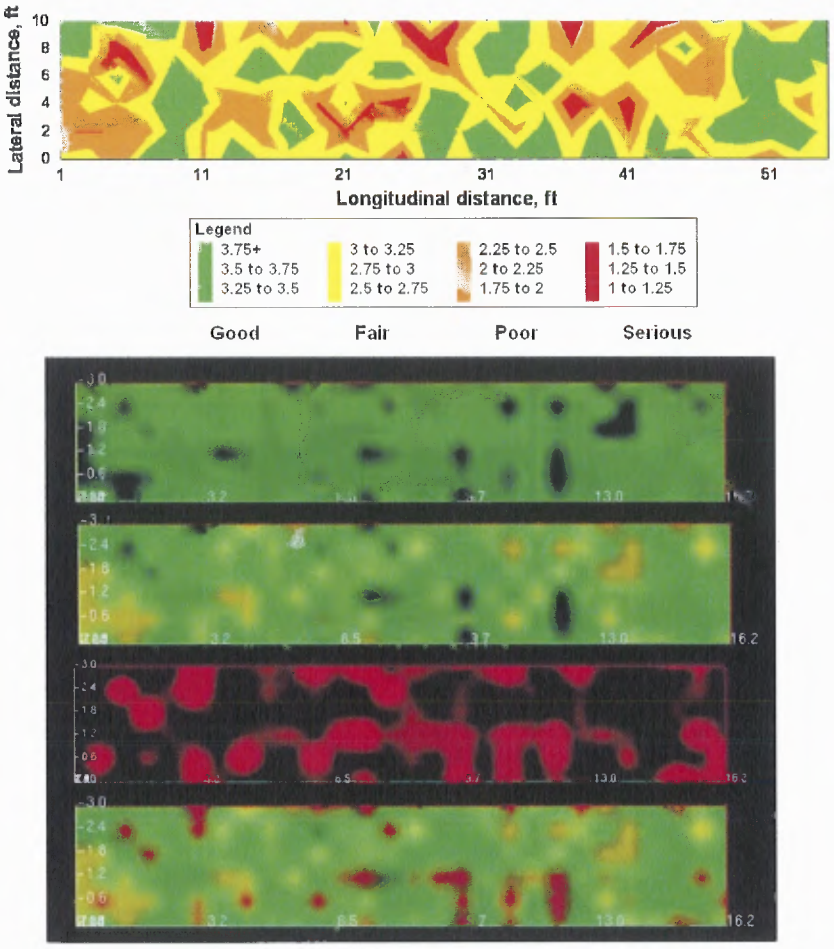

Figure 4.10 Condition assessment of Carter Creek Bridge deck : traditional approach (top), and bottom of the deck, delamination layer, deep reflector layer and combined all reflector layers (bottom).

4.5 Summary

IE can be successfully used in the evaluation and long term monitoring of concrete bridge decks. The monitoring can encompass changes in both material characteristics (primarily elastic moduli), and the deck condition with respect to deterioration caused by corrosion

REFERENCES

Acharya, A., Freise, E., and Greener, E. H. 1970. "Open Circuit Potentials and Microstructure of Some Binary Co-Cr Alloys." *Cobalt (Eng. Ed.)*. 47: 75-80.

Breeman, G., Graichen, F., and Rohlman, A. 1993. "Hip Joint Loading During Walking and Running, Measured in Two Patients." *J. Biomechanics*. 26: 969-990.

Cheal, E. J., Spector, M. and Hayes, W. 1992. "Role of Loads Prothesis Material Properties on the Mechanics of the Proximal Femur After Total Hip Arthroplasty." *J. Orthop. Res.* 10: 405-422.

Crowninshield, R. D., Brand, R. A., Johnston, R. C., and Milroy, J. C. 1980. "The Effect of Femoral Stem Cross-Sectional Geometry on Cement Stresses in Total Hip Reconstruction." *Clin. Orthop. Rel. Res.* 146: 71-77.

Crowninshield, R. D., and Brand, R. A. 1981. "A Physiologically Based Criterion of Muscle Force Prediction in Locomotion." *J. Biomechanics*. 14: 793-801.

Davy, D. T., Kotzer, G. M., Brown, R. H., Heiple, K. G., Goldberg, V. M., Heiple, K. G. Jr., Bertilla, J., and Burstein, A. H. 1988. "Telemetric Force Measurement Across the Hip After Total Hip Arthroplasty." *J. Bone Joint Surg.* 70A: 45-50.

Devine, T. M., and Wulff, J. E. 1976. "The Comparitive Crevice Corrosion Resistance of Cobalt-Chromium Base Surgical Implant Alloys." *J. Electrochem. Soc.* 123: 1433.

Evans, E. M., Freeman, M. A. R., Muller, A. J., and Vernon, R. B. 1974. "Metal Sensitivity as a Cause for Bone Necrosis and Loosening of the Prothesis in Total Joint Replacement." *J. Bone Joint Surg.* 56B: 626.

Halliday, D., and Resnick, R. 1988. "Properties of the Elements." in *Fundamentals of Physics*. ed. J. Merrill. 3rd Ed. New York: John Wiley & Sons. pp. A8.

Hibbeler, R. C. 1994a. "Poisson's Ratio." in *Mechanics of Materials*. ed. W. Stenquist. 2nd Ed. New York: Macmillian College Publishing Co. pp. 105.

_____. 1994b. "Transverse Shear." in *Mechanics of Materials*. ed. W. Stenquist. 2nd Ed. New York: Macmillian College Publishing Co. pp. 369-382.

Hodge, W. A., Carlson, K. L., Fijan, R. S., Burgess, R. G., Riley, P. O., and Harris, W. H. 1989. "Contract Pressures from an Instrumented Hip Endoprosthesis." *J Bone Joint Surg.* 71A: 1378-1386.

Holtzclaw, H. F., Robinson, W. R., and Odom, J. D. 1991. "Preparation of the Transition Metals." in *General Chemistry with Qualitative Analysis.* ed. K. P. Hamann. 9th Ed. Massachusetts: D. C. Heath and Company. pp. 861-867.

Huiskes, R., and Hollister, S. J. 1993. "From Structure to Process, From Organ to Cell: Recent Developments of FE-Analysis in Orthopaedic Biomechanics." *J Biomech. Eng.* 23: 520-527.

Jung, C., Ikonen, T., and Rabah, K. 1997. "Finite Element Study on the Performance of a Modified Hip Implant Used With the Trochanter Cable Grip Assembly." *Department of Mechanical Engineering, New Jersey Institute of Technology.* Newark, NJ.

Juvinall, R. C., and Marshek, K. M. 1991. "Stress Concentration Factors." in *Fundamentals of Machine Component Design.* 2nd Ed. New York: John Wiley & Sons. pp. 128-136.

Kuhn, A. T. 1981. "Corrosion of Co-Cr Alloys in Aqueous Environments." *Biomaterials.* 2: 68-77.

McLeish, R. D., and Charnley, J. 1970. "Abduction Forces in the One-Legged Stance." *J. Biomechanics.* 3: 191-209.

Meachim, G., and Williams, D. F. 1973. "Changes in Nonosseous Tissue Adjacent to Titanium Implants." *J. Biomed. Mat. Res.* 7: 555-572.

Merchant, A. C. 1966. "Hip Abductor Muscle Force." *J. Bone Joint Surg.* 46A: 462-476.

Meriam, J. L., and Kraige, L. G. 1992a. "Equilibrium Conditions." in *Engineering Mechanics: Statics.* ed. C. Robey. 3rd Ed. Vol. 1. New York: John Wiley & Sons. pp. 113-119.

_____. 1992b. "Area Moments of Inertia" in *Engineering Mechanics: Statics.* ed. C. Robey. 3rd Ed. Vol. 1. New York: John Wiley & Sons. pp. 452-467.

Paul, J. P. 1976. "Loading on Normal Hip and Knee Joints and Joint Replacements." in *Advances in Hip and Knee Joint Technology.* ed. M. Schaldach and D. Hohmann. Berlin: Springer-Verlag. pp. 63.

Park, J. B. 1979. "Internal Fracture Fixation Devices." in *Biomaterials.* New York: Plenum Press. pp. 188-190.

Ratner, B. D., Hoffman, A. S., Schoen, F. J., and Lemons, J. E. 1996a. "Characteristics of Biomaterials Science." in *Biomaterials Science: An Introduction to Materials in Medicine.*" New York: Academic Press. pp. 3-7.

_____. 1996b. "Classes of Materials Used in Medicine." in *Biomaterials Science: An Introduction to Materials in Medicine.*" New York: Academic Press. pp. 37-50.

_____. 1996c. "Sutures." in *Biomaterials Science: An Introduction to Materials in Medicine.*" New York: Academic Press. pp. 356-359.

Reddy, J. N. 1993a. "The Basic Concept of the Finite Element Method." in *An Introduction to the Finite Element Method.* ed. J. J. Corrigan and J. M. Morriss. 2nd Ed. New York: McGraw Hill. pp.5-15.

_____. 1993b. "The Basic Concept of the Finite Element Method." in *An Introduction to the Finite Element Method.* ed. J. J. Corrigan and J. M. Morriss. 2nd Ed. New York: McGraw Hill. pp. 70-105.

_____. 1993c. "Basic Steps of the Finite Element Analysis." in *An Introduction to the Finite Element Method.* ed. J. J. Corrigan and J. M. Morriss. 2nd Ed. New York: McGraw Hill. pp. 439-448.

Rohlmann, A., Mossner, U., Bergmann, G., and Kolbel, R. 1983. "Finite Element Analysis and Experimental Investigation in a Femur with a Hip Endoprothesis." *J. Biomechanics.* 16: 727-742.

Rotem, A. 1973 "Effect of Implant Material Properties on the Performance of a Hip Joint Replacement." *J. Med. Eng. Tech.* 8: 208-217.

Tarr, R. R. 1982. "Total Hip Femoral Component Design Stem Characterization, Experimental Studies and Analytical Modeling for the Orthopaedic Surgeon." In *A Scientific Exhibit Presented at the 49th Annual Meeting of the American Academy of Orthopaedic Surgeons.* Department of Orthopedics, University of Southern California and Orthopedic Hospital.

Ugural, A. C., and Fenster, S. K. 1995a. "Principal Stresses in Three Dimensions." in *Advanced Strength and Applied Elasticity.* ed. D. Mosco. 3rd Ed. New Jersey: Prentice Hall, Inc. pp. 31-34.

_____. 1995b. "Engineering Materials." in *Advanced Strength and Applied Elasticity.* ed. D. Mosco. 3rd Ed. New Jersey: Prentice Hall, Inc. pp. 64-65.

_____.1995c. "Contact Stresses." in *Advanced Strength and Applied Elasticity.* ed. D. Mosco. 3rd Ed. New Jersey: Prentice Hall, Inc. pp. 133-139.

_____.1995d. "Maximum Distortion Energy Theory." in *Advanced Strength and Applied Elasticity.* ed. D. Mosco. 3rd Ed. New Jersey: Prentice Hall, Inc. pp. 155-157.

_____.1995e. "Solution of the Stress Cubic Equation." in *Advanced Strength and Applied Elasticity.* ed. D. Mosco. 3rd Ed. New Jersey: Prentice Hall, Inc. pp. 527-528.

_____.1995f. "Internal Force-Resultant and Stress Relations." in *Advanced Strength and Applied Elasticity.* ed. D. Mosco. 3rd Ed. New Jersey: Prentice Hall, Inc. pp. 9-13.

Walker, P. S., and Robertson, D. D. 1988. "Design and Fabrication of Cementless Hip Stems." *Clin. Orthop. Rel. Res.* 235: 25-34.

Williams, D. F. 1977. "Titanium as a Metal for Implantation Part 2: Biological Properties and Clinical Applications." *J Med. Eng. Tech.* 1: 266-270.

Winter, G. D., Leray, J. L., and Groot, K. de. 1980a. "Cobalt-Based Alloys." in *Evaluation of Biomaterials*. Vol. 1. New York: John Wiley & Sons. pp. 106-116.

_____. 1980b. "Suture Materials." in *Evaluation of Biomaterials*. Vol. 1. New York: John Wiley & Sons. pp. 346-353.

_____. 1980c. "Titanium and Titanium Alloys." in *Evaluation of Biomaterials*. Vol. 1. New York: John Wiley & Sons. pp. 360-365.

Zeid, I. 1991. "Finite Element Analysis." in *CAD/CAM Theory and Practice*. ed. J. J. Corrigan and J. M. Morriss. New York: McGraw Hill. pp. 881-918.